**TECHNISCHE
UNIVERSITÄT
WIEN**
Vienna University of Technology

DIPLOMARBEIT

Setup of a Fabry-Pérot Resonator as a Narrow-Band Filter for Atomic Fluorescence Signals

Ausgeführt am

Atominstitut

der Technischen Universität Wien

unter Anleitung von

Prof. Dr. Arno Rauschenbeutel,
Dr. Christoph Clausen und Dr. Philipp Schneeweiß

durch

Daniel Weiss
Rueppgasse 32/13
1020 Wien

Contents

1 Introduction

Optical fibers by now provide an indispensable backbone for the transport of information around the globe and are readily available in large quantities. Besides their technical applications, they can be used to conduct advanced experiments in the field of quantum optics. Such experiments include the transport of atoms through hollow-core fibers [1], their use as fiber Bragg gratings [2, 3] and as gain medium for Raman fiber lasers [4]. This Master thesis was written at the group of Professor Rauschenbeutel, where the interaction of fiber-guided light with atoms [5, 6], molecules [7] and nanoparticles [8] is investigated.

A standard telecommunication-grade optical fiber consists of fused silica (SiO_2) with a very small amount of impurities. Light is guided through a cylindrical core, which is surrounded by a cladding with slightly lower refractive index. This leads to low-loss light propagation by total internal reflection at the boundary [9]. These fibers usually have a core diameter of a few micrometers and an overall diameter of about 125 µm. Since the core diameter is much larger than the wavelength, light propagates mainly in the core with a small evanescent field extending into the cladding.

In our group, we use fibers with sub-wavelength diameters to interface matter with guided light. These fibers are also called nanofibers or tapered optical fiber (TOF). Due to their small dimensions, a significant part of the optical power is transported in the evanescent field. This allows for strong coupling with matter. For example, a single atom, placed in the evanescent field, can easily absorb several percent of the guided light [10].

These nanofibers can be produced by heating a single-mode fiber while pulling on both ends in a well-defined way [11, 12]. The result is an adiabatic transition between fiber and nanofiber with transmissions of 99 % or better. This is shown in figure 1.1.

One big advantage of nanofibers compared to strongly-focussed free-space laser beams is the possibility to have high intensities over comparatively long distances. The interaction of atoms with the evanescent field can be used to trap atoms around the nanofiber [5, 14]. This trap is described in section 3.1 and results in two one-dimensional diametric arrays of trapping potentials. The trapping lasers interact with the molecules of the fiber, which leads to Raman scattering and fluorescence [15]. Ongoing experiments to study electromagnetically-induced transparency (EIT) [16] with trapped cesium atoms use a probe laser on the cesium
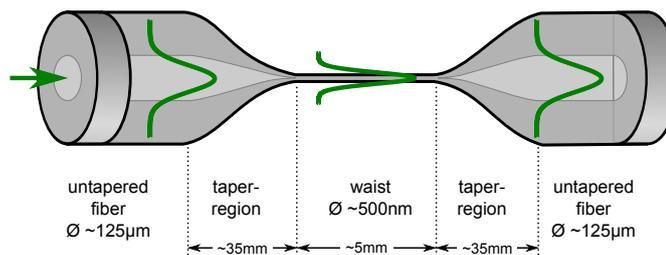
Figure 1.1: Sketch of a tapered optical fiber. Shown is the normal fiber (left and right) with the nanofiber in-between. The intensity distribution of light propagating in the fiber is shown in green. In the taper region, the light transitions from propagating in the core (light gray) to propagating in the cladding (dark gray) and the evanescent field is now in the surrounding vacuum. Note that the relative sizes of core, cladding and nanofiber are not to scale. Figure taken from [13].

D2 line at 852 nm and a 9.2 GHz detuned control laser. To achieve sufficient signal-to-noise ratios, it is necessary to suppress the control laser and filter out the background caused by Raman scattering. Ideally, only the probe field would reach the detector.

There are different approaches of how this filtering could be achieved. The simplest solution would be to use optical filters, such as laser line filters or a combination of short and longpass filters. However, an off-the-shelf laser-line filter has a transmission bandwidth on the order of 1 THz, which is much larger than the frequency spacing between control and probe field. With the current setup, the light is already filtered to a bandwidth of about 50 GHz by reflection on a volume Bragg grating. Much better filtering can be achieved by using a Fabry-Pérot interferometer (FPI) [17].

The first part of this Master's thesis describes the design, setup and characterization of an FPI that is actively stabilized to a reference laser. This FPI offers high transmission of the probe laser and strong suppression of both, the Raman scattered light and the EIT control field. A detailed motivation for this FPI is given in section 2.1 and the design requirements are discussed. In the following sections, the design and the experimental setup as well as the coupling of light to the FPI are described and the actual performance is examined. Finally, the losses inside the FPI are estimated and the stability is evaluated.

The strong suppression of background photons offered by the FPI opens up a range of new experimental possibilities. As an example, the second half of this Master's thesis investigates the accurate estimation of the number of atoms trapped around the nanofiber. With the FPI, it is possible to significantly improve the counting of atoms in the nanofiber-based trap. This is described in chapter 3. The

trap is introduced in section 3.1, followed by a discussion of the scattering of light by trapped atoms and the heating caused by this. Different approaches on how to count the atoms are given in section 3.3 and their performance is evaluated with the help of Monte-Carlo simulations based on current experimental parameters. It is shown that the precision of atom counting improves with the cavity by a factor of 3 for small atom numbers, yielding a standard deviation of about 9 for 30 trapped atoms. Accurate determination of the atom number leads to a loss of almost all trapped atoms due to heating effects. When simultaneously cooling the atoms, single-atom accuracy is possible.

At the end of both chapters, a conclusion is given and a summary can be found in chapter 4.

2 Cavity Filter

Optical resonators are optical components that change the beam path in such a way, that the beam retraces itself multiple times before leaving the resonator. The simplest case is the Fabry-Pérot interferometer (FPI) [17], which consists of two mirrors that are facing each other. Note that throughout this report, the terms resonator, FPI and cavity are used interchangeably. The special case of an FPI with curved mirrors is shown in figure 2.1. The mirrors are partially transmitting,
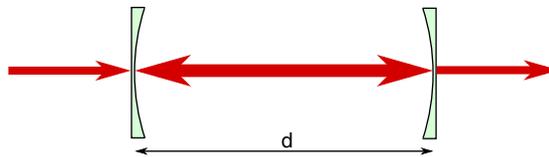
Figure 2.1: Fabry-Pérot resonator with two identical plano-concave mirrors. The arrows indicate light coupled into the resonator from the left, being reflected many times inside the resonator and leaving it to the right. The arrow inside the resonator is drawn larger to indicate the higher intensity with respect to the incident beam (cf. later sections)

so that a light beam can enter the resonator and continues to oscillate between both mirrors multiple times before leaving the resonator through either the first or the second mirror.

In the special case of the beam fulfilling the resonance condition, ideally all of the incoming beam is transmitted through the FPI and none is reflected. The intensity inside the resonator is in general much higher than that of the incident beam. This ideal case is shown in figure 2.1. In reality, losses in the resonator (see section 2.4) and imperfect coupling (cf. section 2.3.8) result in part of the incident beam being reflected by the resonator and diminish the intensity of the transmitted beam. On the other hand, an off-resonant beam leads to high reflection and low transmission at the FPI. This is due to interference of the out-coupled beams after having been trapped in the resonator for various numbers of round trips.

Inside the resonator, a beam is reflected by the mirrors and after each round trip interferes with itself. Only for constructive interference will the resonator transmit the incident beam. This leads to good transmission of discrete frequencies, the so-called resonator modes. These modes can be derived by looking at the propagation

of a plane wave in the resonator with amplitude:

$$A e^{ikz} \, . \tag{2.1}$$

Assuming a distance d between the mirrors, and requiring constructive interference, the wave has to retrace itself after having travelled distance $2d$

$$A e^{ikz} \overset{!}{=} A e^{ik(z+2d)} \tag{2.2}$$

$$\Rightarrow k_n = \frac{n\pi}{d} \tag{2.3}$$

$$\Leftrightarrow \nu_n = n\frac{c}{2d} =: n \cdot \nu_{\mathrm{FSR}} \, , \tag{2.4}$$

where $n \in \mathbb{N}$ and ν is the frequency of the plane wave. We used $k = \frac{2\pi}{\lambda} = \frac{2\pi\nu}{c}$ with λ being the wavelength. The newly-introduced parameter ν_{FSR} is the frequency spacing between the modes and is termed free spectral range (FSR). A more rigorous derivation of resonator modes is given in section 2.3.4. However, this simple result is still valid and gives the spacing for the later termed longitudinal modes.

The linewidth[1] $\delta\nu$ of these modes is highly dependent upon the losses in the resonator and the reflectivity of the mirrors. The relation between the linewidth and the FSR is determined by the *finesse* $\mathcal{F}$

$$\delta\nu = \frac{\nu_{\mathrm{FSR}}}{\mathcal{F}} \, . \tag{2.5}$$

The derivation of expressions for $\mathcal{F}$ and $\delta\nu$ can be found in section 2.3.4. Figure 2.2 illustrates the optical power transmitted through the FPI in dependence of the frequency of the light. The maximal suppression of off-resonant light is also derived in section 2.3.4 and is

$$P_{\mathrm{min}} \propto \mathcal{F}^{-2} \, , \tag{2.6}$$

where P_{min} is the minimal transmitted power (at the center of two peaks in figure 2.2).

This chapter is dedicated to the filtering cavity. First, a motivation of why this cavity is needed and what requirements it should fulfil is given in section 2.1. The design resulting from these requirements is described in section 2.2. Then, the process of coupling light into the cavity as well as actual performance of the cavity are discussed in section 2.3. The effect of losses on the properties of the cavity is outlined in section 2.4 and the complete experimental setup can be found in section 2.5. Finally, the stabilization of the lasers and the cavity as well as their long-term stability are assessed in sections 2.6 and 2.7.

---

[1]full width at half maximum
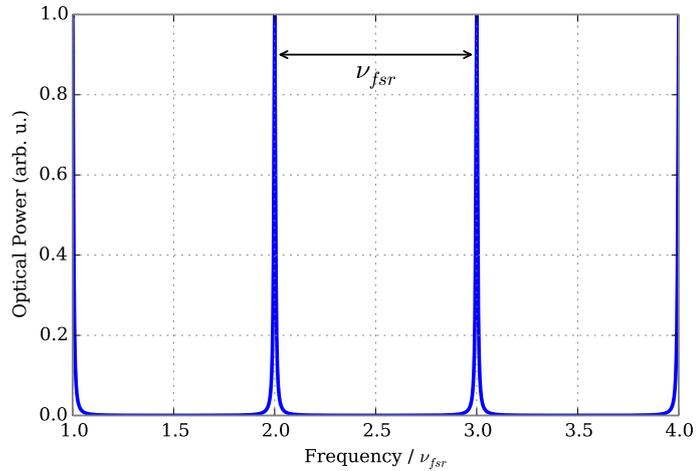
Figure 2.2: Longitudinal modes of an FPI with normalized power and a finesse of 100.

2.1 Motivation and Requirements

The experiment with cesium atoms trapped around an optical nanofiber, at which this cavity will be used, is roughly outlined in chapter 1 and described in more detail in section 3.1. The cavity has two purposes. On the one hand it filters out background light from the fiber that would otherwise interfere with the signal and on the other hand it suppresses the control beam in electromagnetically-induced transparency (EIT) experiments. In the following, both effects are briefly described and resulting requirements for the cavity are deduced in section 2.1.3.

The aforementioned background light is a combination of Raman scattering and fluorescence. A more comprehensive introduction to these effects can be found in literature [18, 19, 20, 21, 22, 23] with emphasis on the thesis of David Wardle [15] that treats the specific case of Raman scattering in optical fibers.

EIT was introduced by [24] in 1986 and first observed by [25] in 1991. A more comprehensive description is given in [16].

2.1.1 Fluorescence and Raman scattering in fibers

When monochromatic light is sent through a fiber, characteristic spectra can be observed that show peaks at higher as well as lower wavelengths than the incident light. This is due to a combination of Raman scattering and fluorescence. These processes are illustrated in figure 2.3. Fluorescence occurs when a photon excites an atom from ground state $|g\rangle$ to an excited state $|e\rangle$ and afterwards the atom
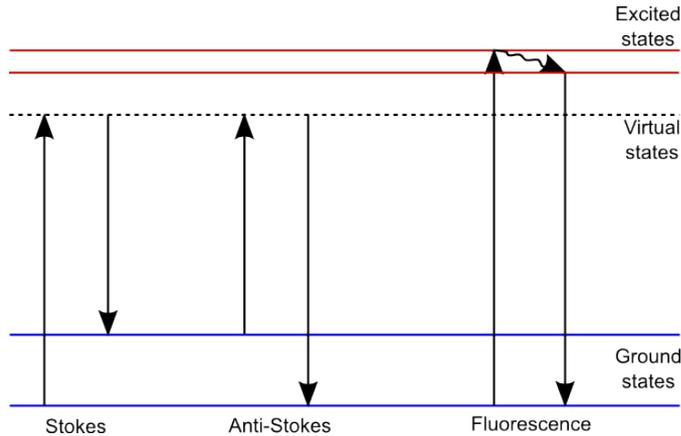
Figure 2.3: Visualization of Raman scattering and Fluorescence. Raman scattering leads to a constant frequency shift to higher (Anti-Stokes) or lower (Stokes) frequencies with respect to the pump light (independent of the pump frequency), while fluorescence results in the emission of photons at fixed frequencies.

first decays to another excited state $|e'\rangle$, before returning to the ground state by emission of a photon. Raman scattering takes place when an incident photon excites an atom from initial state $|i\rangle$ to a virtual state $|v\rangle$, after which the atom decays to final state $|f\rangle$ by emitting a photon. Both, fluorescence and Raman scattering occur when sending light through an optical fiber and lead to detection of unwanted background photons. The intensity of this background light depends highly on the wavelength of the light originally sent through the fiber and the wavelength range of detection.

The cavity can filter out large parts of this background since it only transmits fixed modes and suppresses other frequencies. This is illustrated in figure 2.4. The light from the fiber is already pre-selected by reflection at a volume Bragg grating[2] before arriving at the cavity. Since the frequency range for which the Bragg grating reflects is larger than the FSR of the cavity, more than one cavity mode can be excited by the background light. However, large parts are suppressed as can easily be seen in figure 2.4.

It should be noted that changing the FSR while keeping the finesse fixed does not change the suppression of background light over a wide range around the chosen value of $\nu_{\mathrm{FSR}} = 18.7\,\mathrm{GHz}$ (see section 2.1.3). This is depicted in figure 2.5. An explanation of why this value is chosen for the FSR is given below.

---

[2]Optigrate RBG-852-94
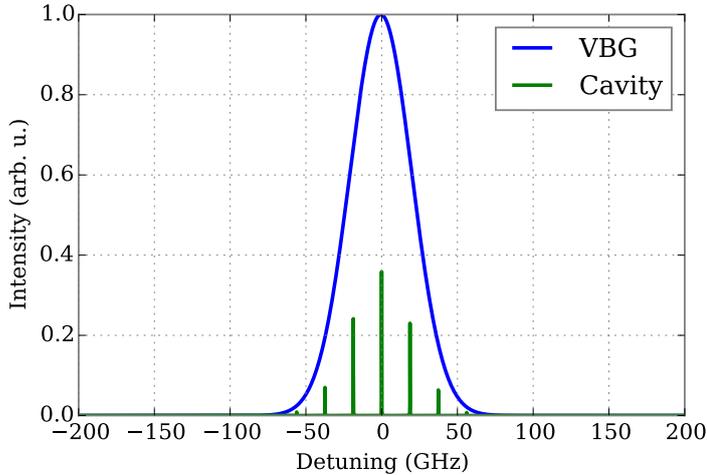
Figure 2.4: The light from the volume Bragg grating (VBG) shows a Gaussian distribution on a frequency axis (blue curve). When subsequently filtered by the cavity, only discreet modes are transmitted and the overall intensity is reduced due to non-perfect transmission through the resonator setup (green curve).

2.1.2 Electromagnetically-Induced Transparency

The main motivation for the cavity is to allow for better measurements of EIT at the nanofiber trap. With EIT, an initially opaque medium can be made transparent by use of a control field. There are various schemes of how this can be realized [16]. At the nanofiber trap, this is done with the Λ-type level scheme that is shown in figure 2.6. A probe field driving the $|F = 3\rangle$-$|F' = 4\rangle$ transition of the cesium D2 line is absorbed by the atoms. When additionally a control field ($|F = 4\rangle$-$|F' = 4\rangle$) is switched on, the two paths $|F = 3\rangle$-$|F' = 4\rangle$ and $|F = 3\rangle$-$|F' = 4\rangle$-$|F = 4\rangle$-$|F' = 4\rangle$ interfere destructively, leading to transparency for the probe field. Furthermore, this leads to a steep change of the refractive index around resonance and thus slow group velocities. This is known as slow light and can be used to store light in the medium and later retrieve it by adiabatically switching the control pulse off and on, respectively.

For good results, it is imperative to maximize detection of the probe beam while ideally not detecting the control beam at all. The frequency difference between the probe and the control field for the scheme shown in figure 2.6 corresponds to the energy difference between the $F = 4$ and $F = 3$ level ground states, which is $\Delta\nu = 9.2\,\text{GHz}$ [26]. As indicated in the introduction of this chapter, the maximal suppression of a resonator is at the center frequencies between two modes. There-
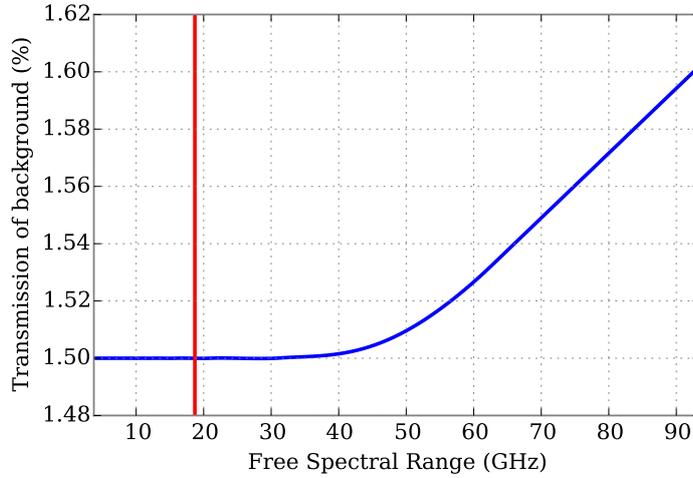
Figure 2.5: Change of background suppression with the FSR.
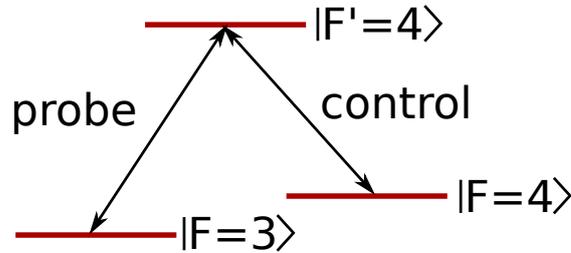
Figure 2.6: Lambda level scheme for EIT. A probe beam drives the $|F = 3\rangle$-$|F' = 4\rangle$ transition and a control field the $|F = 4\rangle$-$|F' = 4\rangle$ transition. In this case, cesium atoms were used and the levels correspond to the hyperfine states of the D2 line.

fore, for optimal suppression of the control beam while maximizing transmission of the probe beam, the FSR has to be $2\Delta\nu = 18.4\,\mathrm{GHz}$.

2.1.3 Requirements for the Cavity

High Transmission

Since the cavity will be used to filter the light of the experiment, it should have good transmission for frequencies of interest and high suppression for all other frequencies. In section 2.4, an equation for the intensity of the transmitted light through the cavity is given. According to equation 2.74, the ideal case of perfect transmission on resonance requires two identical mirrors.

Suppresion of Control Beam

In section 2.1.2, we determined that the FSR should ideally be $18.4\,\text{GHz}$ to best suppress the control field at maximal transmission of the probe field in EIT. This would correspond to a distance between the mirrors of $d = 8.02\,\text{mm}$. To facilitate the setup of the cavity, a nominal distance of $d = 8\,\text{mm}$ is chosen, corresponding to an FSR of $\nu_{\text{FSR}} = 18.7\,\text{GHz}$. Note that the distance between both mirrors will be measured by a calliper and its accuracy is thus about $\pm 0.2\,\text{mm}$. This translates to a possible variation of the FSR of about $\pm 0.5\,\text{GHz}$. With this configuration, the control field is best suppressed but the fraction I_{min} that is still being transmitted depends on the finesse $\mathcal{F}$ of the cavity $I_{\text{min}} \propto \mathcal{F}^{-2}$ (cf. equation 2.6). Therefore, a high finesse is desirable.

Suppression of Background Light

The suppression of background light is discussed in section 2.1.1 and is only dependent upon the finesse of the cavity. The higher the finesse, the better the suppression. This can easily be seen in figure 2.4, since according to equation 2.5 higher finesse results in smaller linewidth. The FSR does not influence this, as changes around the chosen value of $18.7\,\text{GHz}$ do not influence the suppression of the background (cf. figure 2.5). As a result, the finesse should be high to have less background.

Linewidth

Both previous requirements, the suppression of the control field and of the background light, call for a high finesse. The linewidth is coupled to the finesse via the FSR (cf. equation 2.5) and in particular $\delta\nu \propto \mathcal{F}^{-1}$. Thus higher finesse leads to smaller linewidth. However, the linewidth needs to be larger than the linewidth of the probe field to allow for high transmission.

Stability

The cavity should provide constant transmission at the frequency of the probe field and therefore needs to be stabilized with respect to the FSR. This is described in detail in section 2.7.

Fiber-coupled

As a final requirement, the cavity should be fiber-coupled to allow for easy integration into the existing setup and facilitate switching between using the cavity or bypassing it.

2.2 Cavity Design

The cavity is designed to best accommodate the requirements of section 2.1.3. A first requirement was to use identical mirrors and to have a high finesse. In equation 2.40, the finesse $\mathcal{F}$ is linked directly to the reflectivity R of the mirrors $\mathcal{F} \approx \frac{\pi}{1-\sqrt{R}}$. Thus, for high finesse, the reflectivity needs to be close to 1.

There were already plano-concave mirrors available with reflectivities of 98.54 %[3]. This gives a nominal finesse of 214 (cf. equation 2.40). The linewidth for transmission is then 88 MHz (cf. equation 2.5), which is larger than the linewidth of the probe field.

Another requirement was an FSR of 18.7 GHz. This translates to a distance between the mirrors of 8 mm. To be able to adjust this distance, the mirrors are mounted on a slide rail as shown in figure 2.7. This allows to change the distance
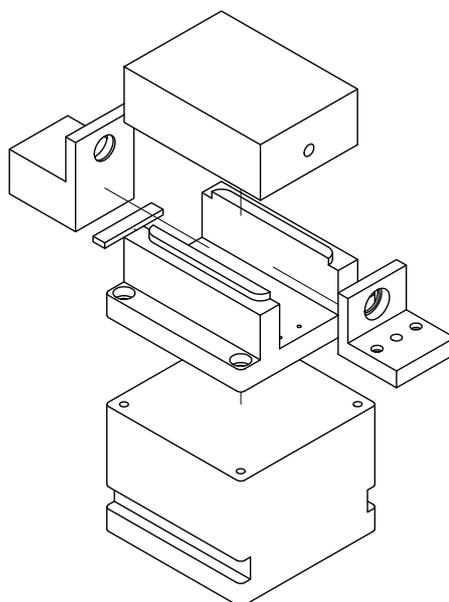
Figure 2.7: Exploded view of the cavity mount. The mirrors are placed in the holes of the two mounts in the slide rail. A plastic cap covers the setup to minimize disturbances and to protect the mirrors from dust. The mirror mount to the right is placed on a translation stage (not shown).

over a range of multiple millimetres. One of the mirrors is additionally mounted on a translation stage[4] to fine-tune this distance with a micrometre screw over a range of about 1.5 mm. Finally, a built-in piezo crystal allows for very fine adjustments

---

[3]LENS-Optics PR780-1064nm/0°, BK7, Radius: −50 mm
[4]Thorlabs Nano Flex Translation Stage Metric (NF15AP25/M)

within a range of 25 µm and a resolution of 10 nm. This fine-tuning is necessary to ensure that the cavity can be stabilized to a reference laser while maintaining maximal transmission of the probe light. A detailed description of this process is given in section 2.7.

2.3 Coupling into the Cavity

This section describes the coupling of light into the cavity and gives the performance of the cavity with respect to the requirements of section 2.1.3.

First, a convenient way to describe the propagation of paraxial light through optical components is discussed in section 2.3.1. The concept of Gaussian beams is introduced in section 2.3.2, followed by a discussion of possible cavity modes (section 2.3.4) and a more rigorous introduction to FSR, finesse and linewidth. Then, the actually measured properties are presented and the process of matching incident light to specific modes is described in section 2.3.8. Finally, the efficiency of the coupling is given in section 2.3.11.

2.3.1 Ray Optics

In the paraxial ray approximation[5], $\sin(\phi) \approx \phi$, and under the premise that rays only propagate in a single plane, a coordinate system can be found, in which they are fully described by their position along the y axis and their angle ϕ with respect to the optical axis (see figure 2.8). Optical components can then be represented by a 2x2 matrix called *ray transfer matrix* [27].
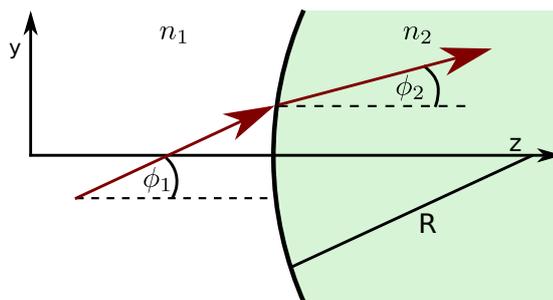
Figure 2.8: Rays propagating in positive z direction can be fully characterized by their angle ϕ with the optical axis (z axis) and their distance y from the z axis. Any optical component might change the ray's coordinates (y, ϕ).

---

[5]All light rays propagate at small angles with respect to the optical axis.

12

Ray propagation is in the following always assumed to be in the positive z direction. Any optical component alters the beam path described by (y_1, ϕ_1), so that it afterwards has different coordinates (y_2, ϕ_2), which are determined by Snell's law (already in the paraxial approximation)

$$\frac{\phi_1}{\phi_2} = \frac{n1}{n2} .\tag{2.7}$$

The change in coordinates by the optical component can be expressed by a matrix equation

$$\underbrace{\begin{pmatrix} A & B \\ C & D \end{pmatrix}}_{=:M} \begin{pmatrix} y_1 \\ \phi_1 \end{pmatrix} = \begin{pmatrix} y_2 \\ \phi_2 \end{pmatrix} .\tag{2.8}$$

The so-defined matrix M is the ray transfer matrix. Free propagation can also be described by a ray transfer matrix, so that $(y(z_2), \phi(z_2)) = M(y(z_1), \phi(z_1))$.

These matrices provide a very versatile tool to easily describe sequences of optical components. Two components that are traversed by the same ray in direct succession can then be expressed as

$$\underbrace{\begin{pmatrix} E & F \\ G & H \end{pmatrix} \begin{pmatrix} A & B \\ C & D \end{pmatrix}}_{\tilde{M}} \begin{pmatrix} y_1 \\ \phi_1 \end{pmatrix} = \begin{pmatrix} y_2 \\ \phi_2 \end{pmatrix} \tag{2.9}$$

where $\tilde{M}$ represents the ray transfer matrix for the system of both components. A short list of ray transfer matrixes needed in later sections is given in table 2.1, a more exhaustive list can be found in [27].

Note that for all ray transfer matrices M, the determinant is [28]

$$\det(M) = \frac{n_1}{n_2} ,\tag{2.10}$$

where n_1 is the refractive index of the medium before the optical component and n_2 after. Ray optics leads to vanishing spot sizes at focal points, which is not physical. Another way to describe light beams, which additionally takes into account beam divergence and the existence of a diffraction limit, is introduced in the next section.
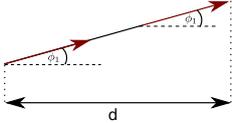
	$\begin{pmatrix} 1 & d \\ 0 & 1 \end{pmatrix}$	Free-space propagation
	$\begin{pmatrix} 1 & 0 \\ 0 & \frac{n_1}{n_2} \end{pmatrix}$	Refraction at planar boundary
	$\begin{pmatrix} 1 & 0 \\ -\frac{n_2-n_1}{n_2 R} & \frac{n_1}{n_2} \end{pmatrix}$	Refraction at spherical boundary
	$\begin{pmatrix} 1 & 0 \\ -\frac{1}{f} & 1 \end{pmatrix}$	Transmission through a thin lens
	$\begin{pmatrix} 1 & 0 \\ \frac{2}{R} & 1 \end{pmatrix}$	Reflection at spherical mirror
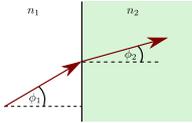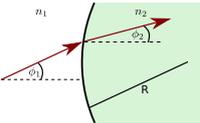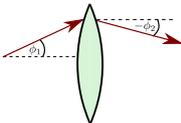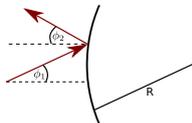
Table 2.1: Some important ray transfer matrices that will be used in later sections. Note that the focal length f is positive and the radii R are defined as positive if the ray impacts on a convex boundary and negative for concave boundaries.

2.3.2 Gaussian Beams

The concept of Gaussian beams is very powerful in describing the properties of light beams (e.g. those emitted by a laser). It is based on the idea that the intensity distribution in any plane perpendicular to the direction of propagation can be described by a two-dimensional Gaussian as illustrated in figure 2.9. Figure
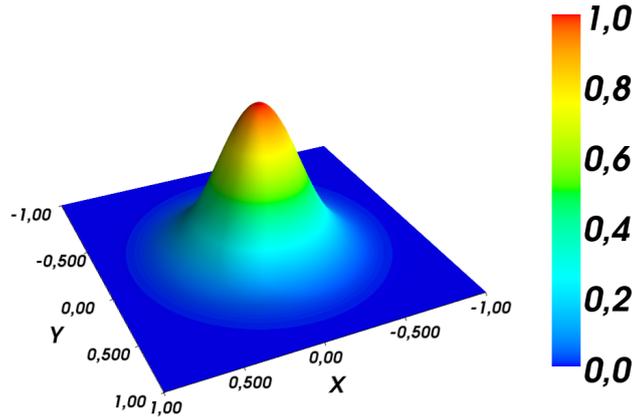
Figure 2.9: Shown is a two-dimensional Gaussian that describes the intensity distribution of a Gaussian beam. The normalized intensity is shown on the z-axis, while the x- and y-axes define a plane perpendicular to the direction of propagation. The beam's center is at position $(x = 0, y = 0)$.

2.10 shows the sketch of a Gaussian beam that propagates along the z axis. The waist is the beam radius at its smallest extension with the radius being defined as the distance from the optical axis to where the intensity has dropped to $\frac{1}{e^2}$ of the maximal intensity (W_0 in figure 2.10). The position of the waist along the optical axis (z-axis) is defined as $z = 0$. The Rayleigh length z_0 is defined as the distance from the waist to where the area of the beam has doubled. Note that a Gaussian beam is completely characterized by the Rayleigh length and the wavelength of the light (see equation 2.20 and the following).

Mathematically, Gaussian waves are one possible solution to the paraxial Helmholtz equation, as will be outlined in the following. Electromagnetic waves are governed by the wave equation (in free space)

$$\left(\nabla^2 - \frac{1}{c^2} \frac{\partial^2}{\partial t^2} \right) u(\vec{r}, t) = 0 \,, \tag{2.11}$$

which can be solved by separation of variables

$$u(\vec{r}, t) = E(\vec{r}) T(t) \,. \tag{2.12}$$
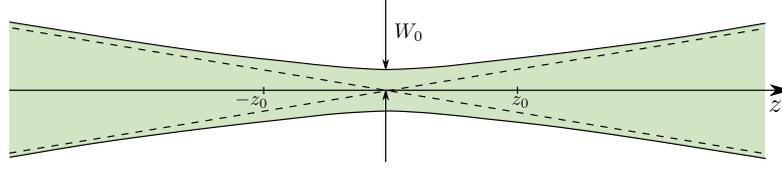
Figure 2.10: Sketch of a Gaussian beam. The minimal radius of the beam is called waist and denoted W_0. The position of the waist is defined as $z = 0$. The distance to where the area of the beam is $\sqrt{2}W_0$ is called Rayleigh length z_0 (see text).

This leads to

$$\frac{\left(\nabla^2 - \frac{1}{c^2}\frac{\partial^2}{\partial t^2}\right) E(\vec{r})}{E(\vec{r})} = \frac{\left(\nabla^2 - \frac{1}{c^2}\frac{\partial^2}{\partial t^2}\right) T(t)}{T(t)} =: k^2 \,. \tag{2.13}$$

Since the first term only depends on position $\vec{r}$ and the second only on the time t, they must both be constant and their value is chosen as k^2 with $k = \frac{2\pi}{\lambda}$ being the wavenumber as will become clear later. λ is the wavelength of the beam.

The time-dependent part can thus be written as

$$\left(k^2 - \frac{1}{c^2}\frac{\partial^2}{\partial t^2}\right) T(t) = 0 \tag{2.14}$$

with the straightforward solution

$$T(t) = T_0 e^{-i\omega t} \tag{2.15}$$

with $\omega = kc$. The position-dependent part is called Helmholtz equation

$$\left(\nabla^2 + k^2\right) E = 0 \,, \tag{2.16}$$

which for paraxial waves can be approximated with the paraxial Helmholtz equation [28, 29]

$$\left(\frac{\partial^2}{\partial x^2} + \frac{\partial^2}{\partial y^2}\right) E - 2ik\frac{\partial E}{\partial z} = 0 \,. \tag{2.17}$$

One solution to equation 2.17 are the Gaussian waves, which can be written as the product of a plane wave propagating along the z-axis, and a complex envelope $A(\vec{r})$, which is slowly varying with z,

$$E(\vec{r}) = A(\vec{r})e^{-ikz} \tag{2.18}$$

with

$$A(\vec{r}) = \frac{A_1}{q(z)}e^{-ik\frac{\rho^2}{2q(z)}} \,. \tag{2.19}$$

16

In equation 2.19, $\rho = \sqrt{x^2 + y^2}$ is the radial distance from the z-axis, $q(z) = z + iz_0$ is the so-called q-parameter or complex beam parameter and z_0 is the Rayleigh length.

By defining $R(z)$ to be the wavefront radius of curvature and $W(z)$ as the radius of the beam, $q(z)$ can be written as [28]

$$\frac{1}{q(z)} = \frac{1}{R(z)} - i\frac{\lambda}{\pi W^2(z)} \,, \tag{2.20}$$

with

$$R(z) = z\left[1 + \left(\frac{z_0}{z}\right)^2\right] \tag{2.21}$$

and

$$W(z) = W_0\sqrt{1 + \left(\frac{z}{z_0}\right)^2}. \tag{2.22}$$

The waist radius is given by

$$W_0 = \sqrt{\frac{\lambda z_0}{\pi}}. \tag{2.23}$$

Inserting equation 2.20 into 2.19 and subsequently into 2.18 results in

$$E_{0,0}(\vec{r}) = A_{0,0}\frac{W_0}{W(z)}e^{-\frac{\rho^2}{W^2(z)}}e^{-ikz\ -ik\frac{\rho^2}{2R(z)}+i\zeta(z)} \,, \tag{2.24}$$

where $\zeta(z) = \arctan\left(\frac{z}{z_0}\right)$ is the Gouy phase [30], which results from the finite extent of Gaussian beams [31]. The Gouy phase leads to an overall phase shift of π between $z \to -\infty$ and $z \to +\infty$.

The notation with the indices $_{0,0}$ is chosen to be consistent with the introduction of Hermite-Gaussian waves in the next section. Equation 2.24 gives the complete description of the Gaussian wave when multiplied with $T(t)$ (eq. 2.15).

Analogous to the previous chapter, the effects of optical components on Gaussian beams may be described using the matrices listed in table 2.1. Exactly like shown in equation 2.9, a succession of optical components can be combined to a single matrix

$$M = \begin{pmatrix} A & B \\ C & D \end{pmatrix}. \tag{2.25}$$

To calculate the effect of this optical component on a Gaussian beam, the ABCD law can be used [28]

$$q_2 = \frac{Aq_1 + B}{Cq_1 + D} \,, \tag{2.26}$$

where A, B, C and D are the matrix elements (cf. equation 2.25) and q_1, q_2 refer to $q(z)$ (cf. equation 2.20) before and after passing through the optical component,

respectively. It is then possible to extract beam radius and wavefront curvature from q_2 by looking at the real or imaginary part.

2.3.3 Hermite-Gaussian Beams

As mentioned before, the Gaussian beam is just one possible solution of the paraxial Helmholtz equation. It can be generalized to the Hermite-Gaussian beams, which include the Gaussian beam as their most fundamental solution. They are given by [28]

$$E_{l,m}(\vec{r}) = A_{l,m}\frac{W_0}{W(z)}\mathbb{H}_l\left(\frac{\sqrt{2}x}{W(z)}\right)\mathbb{H}_m\left(\frac{\sqrt{2}y}{W(z)}\right)e^{-\frac{\rho^2}{W^2(z)}}e^{-ikz-ik\frac{\rho^2}{2R(z)}+i(l+m+1)\zeta(z)}$$

(2.27)

$$= A_{l,m}\mathbb{H}_l\left(\frac{\sqrt{2}x}{W(z)}\right)\mathbb{H}_m\left(\frac{\sqrt{2}y}{W(z)}\right)e^{i(l+m)\zeta(z)}\frac{E_{0,0}(\vec{r})}{A_{0,0}},$$

(2.28)

where $\mathbb{H}_l$ and $\mathbb{H}_m$ are Hermite polynomials and l, m are scalars defining the amplitude distribution.

As can be seen from equation 2.28, the difference to the Gaussian beam amplitude $E_{0,0}(\vec{r})$ consists of a change in the amplitude distribution due to the hermite polynomials (see figure 2.11) and an overall phase shift, but the beam diameter as well as the radius of curvature of the wavefronts are always identical with the Gaussian beam. One therefore speaks of modes of the beam, characterised by l, m and written as TEM_{lm} (Transverse Electro-Magnetic). Since $\mathbb{H}_0(x) = 1\,\forall x$, $E_{l,m}$ reduces to the Gaussian beam for $l = 0$, $m = 0$.

2.3.4 Resonator Modes

Any electromagnetic wave propagating between the two mirrors of a resonator is reflected many times. After each round trip, it interferes with itself and only leads to significant intensities within the resonator in case of constructive interference. This corresponds to an accumulated total phase shift per round-trip of $2n\pi$ with $n \in \mathbb{N}$.

From equation 2.27, the condition

$$2n\pi = 2kd - 2(l + m + 1)\Delta\zeta$$

(2.29)

can be extracted for constructive interference after one round-trip with d being the distance between the mirrors and $\Delta\zeta = \zeta(z_1) - \zeta(z_0)$, where z_0 is the positon of the first mirror and z_1 the position of the second mirror. The factor 2 in front of the $\Delta\zeta$ term stems from the fact that the wave accumulates twice the Gouy phase shift when travelling back and forth inside the resonator before retracing itself.
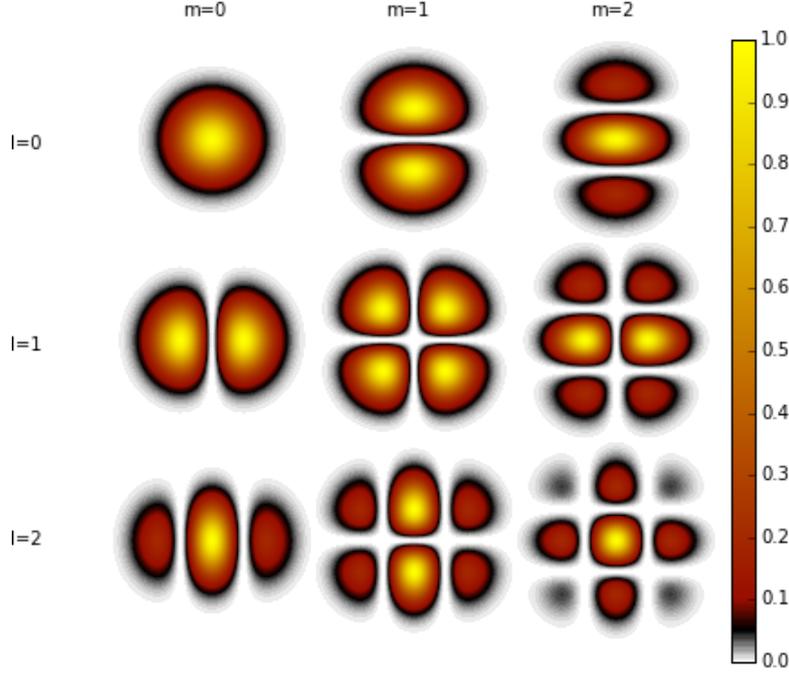
Figure 2.11: Visualization of Hermite-Gaussian modes of a resonator. Shown are the normalized color-coded intensity cross-sections of the beam.

With $k = \frac{2\pi}{\lambda} = \frac{2\pi\nu}{c}$ and solving for ν, we obtain

$$
\begin{aligned}
\nu_{l,m,n} &= \frac{nc}{2d} + (l + m + 1)\frac{\Delta\zeta}{2\pi d} \\
&= n\nu_{\text{FSR}} + (l + m + 1)\frac{\Delta\zeta}{\pi}\nu_{\text{FSR}} \, .
\end{aligned}
\tag{2.30}
$$

The newly introduced variable

$$
\nu_{\text{FSR}} = \frac{c}{2d}
\tag{2.31}
$$

is called free spectral range (FSR). The phase-shift due to reflection at the two mirrors adds up to 2π and can be neglected. This leads to a frequency spacing of ν_{FSR} between two modes of equal (l, m). These modes are called longitudinal modes, as they do have the same amplitude distribution but different frequencies.

Modes of equal n and $l' + m' = l + m$ have the same resonance frequency. In general, the frequency spacing between modes with fixed n is $[(l + m) - (l' + m')]\frac{\Delta\zeta}{\pi}\nu_{\text{FSR}}$. These modes are called transverse modes (see figure 2.11), as they show different amplitude distributions. There are thus theoretically an infinite amount of discrete

19

modes that can be sustained by the resonator (see figure 2.12). In practice, though, these are limited by the dimensions of the cavity mirrors. Note that the FSR is only dependent on the distance between the mirrors and in particular independent of the frequency.
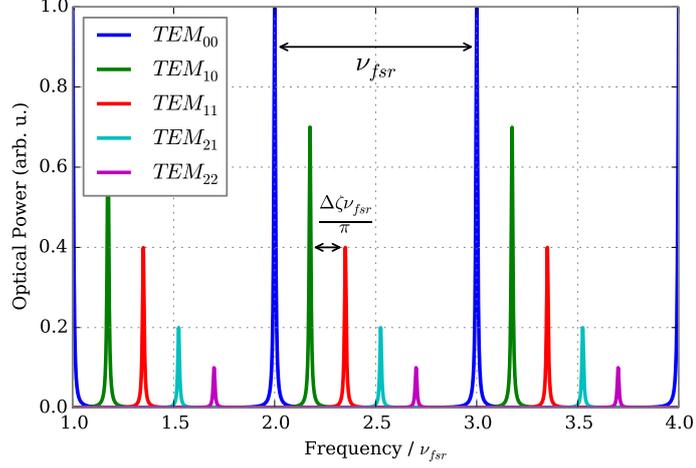
Figure 2.12: Example of coupling to the fundamental mode (TEM$_{00}$) as well as higher-order modes. The frequency spacing between the fundamental modes is the FSR and between higher-order modes with $(l + m - l' - m') = j$ is $j\frac{\Delta\zeta\nu_{\text{fsr}}}{\pi}$. The relative frequency spacings are chosen to match the ones of the cavity used in this report and the relative strength of the transverse modes is arbitrarily scaled.

Considering only the fundamental mode ($l = m = 0$), the wave, characterized by complex amplitude $E_{0,0}(\vec{r})$, accumulates a phase-shift of

$$\Delta\phi = 2kd - 2\Delta\zeta = 4\pi\nu\frac{d}{c} - 2\Delta\zeta \tag{2.32}$$

(cf. equation 2.29) every round trip and its amplitude is attenuated by a factor β ($0 < \beta < 1$) due to losses at reflection and partial transmissivity of the mirrors. After n round-trips, the amplitude has thus changed to

$$E_n = \left(\alpha e^{-i\Delta\phi}\right)^n E_0 =: \xi^n E_0 \,, \tag{2.33}$$

where $\alpha = (1 - \beta)$. The superposition of all E_n gives the total amplitude within the resonator

$$E = \sum_{n=0}^{\infty} E_n = \sum_{n=0}^{\infty} \xi^n E_0 = \frac{E_0}{1 - \xi} \,. \tag{2.34}$$

20

Thus, the internal intensity $|E|^2$ of the resonator can be expressed as

$$I = \frac{|E_0|^2}{(1 - \alpha e^{-i\Delta\phi})(1 - \alpha e^{i\Delta\phi})} = \frac{I_0}{1 - 2\alpha\cos(\Delta\phi) + \alpha^2} \ . \tag{2.35}$$

With

$$\cos(\Delta\phi) = 1 - \sin^2\left(\frac{\Delta\Phi}{2}\right) \ ,$$

the denominator of equation 2.35 becomes

$$1 - 2\alpha + \alpha^2 + 4\alpha\sin^2\left(\frac{\Delta\Phi}{2}\right)$$

$$= (1 - \alpha)^2 + 4\alpha\sin^2\left(\frac{\Delta\Phi}{2}\right)$$

$$= \beta^2\left[1 + \left(\frac{2\sqrt{\alpha}}{1 - \alpha}\right)^2\sin^2\left(\frac{\Delta\Phi}{2}\right)\right] \ ,$$

which leads to

$$I = \frac{I_{\text{max}}}{1 + \left(\frac{2\mathcal{F}}{\pi}\right)^2\sin^2\left(\frac{\Delta\Phi}{2}\right)} = \frac{I_{\text{max}}}{1 + \left(\frac{2\mathcal{F}}{\pi}\right)^2\sin^2\left(\frac{\pi\nu}{\nu_{\text{FSR}}} - \Delta\zeta\right)} \tag{2.36}$$

with the definitions

$$\mathcal{F} := \frac{\pi\sqrt{\alpha}}{1 - \alpha} \ , \tag{2.37}$$

$$I_{\text{max}} := \frac{I_0}{\beta^2} \ . \tag{2.38}$$

$\mathcal{F}$ is called *finesse* and gives a measure of the "quality" of the resonator. This becomes clear when remembering that $\beta = (1 - \alpha)$ is the overall round-trip attenuation of the wave's amplitude and thus for low losses, α is close to 1 and $\mathcal{F} \gg 1$. Furthermore, higher finesse values lead to smaller linewidths and lower intensities at off-resonant frequencies (cf. equation 2.36). In general, α can be written as

$$\alpha = r_1 r_2 \tag{2.39}$$

with the reflectivities r_1, r_2 of the two mirrors and neglecting the attenuation of propagation in air as well as losses inside the resonator. The finesse then becomes

$$\mathcal{F} = \frac{\pi\sqrt{r_1 r_2}}{1 - r_1 r_2} \ . \tag{2.40}$$

21

r_1 and r_2 are the mirror reflectivities with respect to the complex amplitude and thus the square root of the measurable intensity reflectivity R_i.

The maximal intensity follows directly from equation 2.36 and is given in 2.38. To get the minimal intensity, the sine term in equation 2.36 needs to be 1. This results in

$$I_{\text{min}} = \frac{I_{\text{max}}}{1 + \left(\frac{2\mathcal{F}}{\pi}\right)^2} \tag{2.41}$$

and shows that good suppression of unwanted frequencies requires a high finesse, in fact $I_{\text{min}} \propto \mathcal{F}^{-2}$. This is consistent with the fact that the finesse depends on the reflectivity of the mirrors. In the extreme case where $r_1 = r_2 = 0$, the finesse would be 0 as well and the intensity would be I_{max} for all frequencies (perfectly transparent medium). On the other hand, perfect reflectivity of the mirrors results in $\mathcal{F} \to \infty$ and thus infinitely sharp modes with $I_{\text{min}} \to 0$. However, due to the perfect reflectivity, no light could then be coupled in or out of the resonator.

Finally, the linewidth of an intensity peak can be found by setting $I = \frac{I_{\text{max}}}{2}$, which leads to

$$\sin^2\left(\frac{\pi\nu}{\nu_{\text{FSR}}} - \Delta\zeta\right) = \left(\frac{\pi}{2\mathcal{F}}\right)^2. \tag{2.42}$$

With the assumption $\mathcal{F} \gg 1$, which is the case for the cavity discussed in this report, we obtain with the small-angle approximation $(\sin(x) \approx x)$

$$\nu \approx \frac{\nu_{\text{FSR}}}{2\mathcal{F}} + \nu_0 \tag{2.43}$$

with

$$\nu_0 := \Delta\zeta \frac{\nu_{\text{FSR}}}{\pi}. \tag{2.44}$$

Since the intensity I takes its maximal value I_{max} for $\sin\left(\frac{\pi\nu}{\nu_{\text{FSR}}} - \Delta\zeta\right) = 0$, which is true for $\nu = \nu_0$, it follows that the full width at half maximum (FWHM) $\delta\nu$ is twice the difference between 2.43 and ν_0

$$\delta\nu \approx \frac{\nu_{\text{FSR}}}{\mathcal{F}}. \tag{2.45}$$

Note that equation 2.45 is often used as definition of the finesse. The FWHM can also be expressed by the photon lifetime τ as $\delta\nu = \frac{1}{2\pi\tau}$ [28]. This allows the calculation of the mean number of round trips N_{RT} of a photon in the resonator

$$N_{\text{RT}} = \frac{c}{2d}\tau = \nu_{\text{FSR}}\tau = \mathcal{F}\delta\nu\tau = \frac{\mathcal{F}}{2\pi}, \tag{2.46}$$

which is directly proportional to the finesse.

We conclude that higher reflectivity of the mirrors, or lower losses in general, result in sharper peaks, higher maximal intensity inside the cavity and better suppression of off-resonant frequencies.

2.3.5 Free Spectral Range

The FSR is measured by sending light from a tunable laser[6] through the cavity and measuring the transmission. Since the FSR is the frequency difference between longitudinal modes, the laser is only coupled to the fundamental mode of the cavity. The coupling process is discussed in section 2.3.8. To determine the frequency of the laser, its beam is split and one part coupled into the cavity while the other part is routed to a wavelength meter[7]. The setup is sketched in figure 2.13.
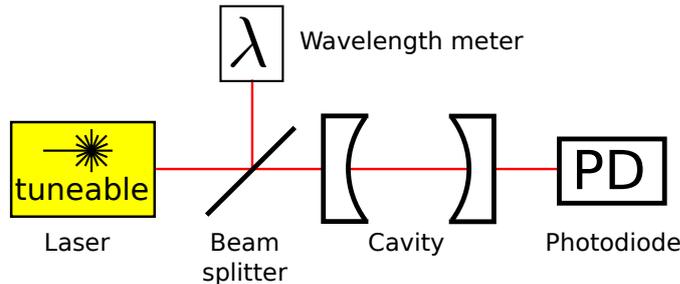
Figure 2.13: Sketch of the setup to measure the FSR. The tuneable laser is coupled into the cavity and the transmission measured with a photodiode. At the same time, the frequency of the laser is measured with a wavelength meter. Note that this setup is just a sketch and is missing the coupling mirrors as well as the coupling lens (cf. section 2.3.8).

The laser is then scanned over a large frequency interval while simultaneously recording the transmission through the cavity and the wavelength of the laser. This results in data as shown in figure 2.14. The FSR can then be calculated as

$$\nu_{\mathrm{FSR}} = \frac{\Delta \nu}{N - 1},$$ (2.47)

where $\Delta \nu$ is the frequency difference between the first and the last recorded peak, and N is the number of peaks. The bigger the frequency interval is, the more accurate the result will be. In practice, the interval is limited by the scan range of the laser and the filters placed in the setup. These filters are described in section 2.5 and were not removed for this measurement to not change the coupling of the cavity.

The signal from the wavelength meter and the transmission through the cavity are recorded independently. To get the correct frequency interval $\Delta \nu$ between first and last peak, we make use of the linearity of the frequency change of the laser. By fitting a straight line to the change of frequency over time (cf. figure 2.14), we

---

[6]Newport New Focus TLB-6300 Velocity Widely Tunable Laser
[7]HighFinesse WS6/600
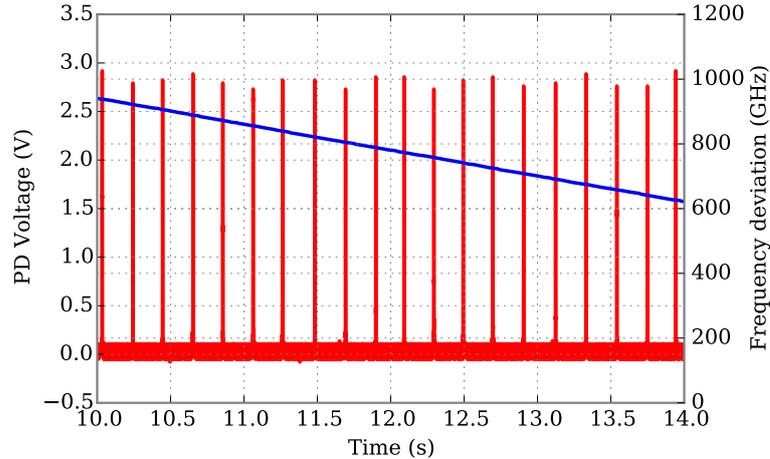
Figure 2.14: Transmission of the cavity while scanning the laser frequency. The intensity of the transmitted light is measured with a photodiode and shown in red. Since the laser is coupled to the fundamental mode, the distance between two peaks, when converted to frequency, corresponds to the FSR. The straight blue line gives the frequency deviation from the end of the scan range. Note that the different heights of the peaks are due to fluctuations in the laser intensity while scanning and not to the sampling size. There are enough measurement points per peak to reliably resolve the intensity maximum.

obtain the change of frequency per unit time $\frac{d\nu}{dt}$. Multiplying this value by the time interval Δt between first and last peak gives the frequency interval $\Delta\nu = \frac{d\nu}{dt}\Delta t$. The positions of the first and last peak are found by fitting Lorentzians.

This has been done in five measurements over frequency intervals of about 1.1 THz. The results are shown in table 2.2 and yield an FSR of

$$\nu_{\mathrm{FSR}} = 16.42\,\mathrm{GHz}\,. \tag{2.48}$$

There is a discrepancy between the measured value and the intended value of 18.7 GHz (cf. section 2.2). The stabilization of the cavity caused many problems in the beginning and there were many adjustments of the distance between the mirrors while trying to solve this problem. Since the measurement of the FSR took place when the cavity was already installed in the main setup, this mismatch was unknown before. Correcting this by adjusting the distance between the mirrors would require the lengthy procedure of aligning the cavity, optimizing the coupling and the position of the coupling lenses to be performed anew. It was shown in section 2.1.1 that a change in the FSR such as this has no effect on the suppression of the background from the fiber. It does, however, affect the suppression of

Frequency Difference (GHz)	Number of Peaks	FSR (GHz)
1083	67	16.41
1100	68	16.42
1101	68	16.43
1100	68	16.42

Table 2.2: Measurements of the FSR with a tuneable laser. Shown are the frequency difference between first and last transmission peak, the number of peaks and the resulting FSR. All scans are centered around 852 nm.

the control field (cf. section 2.1.2). With an FSR of 18.7 GHz, as intended, this suppression would be -43.0 dB. With $\nu_{\mathrm{FSR}} = 16.42$ GHz, it is -42.9 dB. A calculation of the suppression of the control field in dependence of the FSR is shown in figure 2.15. Since this difference is very small, the FSR is left as it is but it should be noted that a small improvement is still possible.

2.3.6 Linewidth

The linewidth of a transmission peak is measured analogously to the FSR (cf. section 2.3.5). However, since the linewidth is on the order of 100 MHz, the measurement needs to be more precise. This is achieved by not using the widely tuneable laser like for the FSR measurement, but the very stable probe laser of the main experiment and modulating its frequency with an acousto-optical modulator (AOM). A scan over a transmission peak is shown in figure 2.16. Fitting a Lorentzian to this peak yields

$$\delta\nu = (73.50 \pm 0.27)\,\mathrm{MHz}\,. \tag{2.49}$$

Note that the curve is slightly asymmetric. When measuring the signal without cavity, significant changes with frequency can be observed. This is due to the changing diffraction efficiency of the AOM and is corrected for in the graph. The reason for the observed asymmetry could be that these corrections are inaccurate. Performing the measurement anew might yield better results.

2.3.7 Finesse

According to equation 2.45, the finesse $\mathcal{F}$ is the ratio of the FSR ν_{FSR} to the linewidth $\delta\nu$. When using the FSR and linewidth given above, we obtain a finesse of

$$\mathcal{F} = \frac{\nu_{\mathrm{FSR}}}{\delta\nu} = 223 \pm 1\,. \tag{2.50}$$
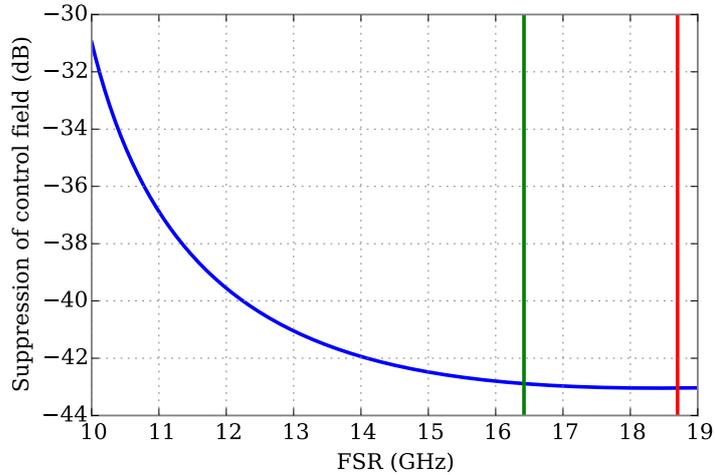
Figure 2.15: Suppression of the control field in EIT when transmission is maximized for the probe field. The calculation is based on equation 2.36 and the frequency spacing between control field and probe field is 9.2 GHz (cf. section 2.1.2). A finesse of 223 is assumed (cf. section 2.3.7). The two vertical lines mark the actual FSR of 16.42 GHz (green) and the ideal FSR of 18.7 GHz (red).

Alternatively, it can be expressed by the reflectivities of the cavity mirrors if neglecting losses inside the resonator (cf. equation 2.40). The intensity reflectivities of the mirrors are measured independently as $R_1 = 0.9887 \pm 0.0051$ and $R_2 = 0.9828 \pm 0.0023$ and correspond well with the nominal value of $R = 0.9854$ given in the datasheet. Thus, the finesse becomes

$$\mathcal{F} = \frac{\pi \sqrt[4]{R_1 R_2}}{1 - \sqrt{R_1 R_2}} = 219 \pm 43 \,, \tag{2.51}$$

with $R_i = r_i^2$ and neglecting losses. Note that the uncertainty is large in this case because the denominator in equation 2.40 is very close to 0. Due to this, the small uncertainties of the reflectivities have a large effect. Both values agree very well within the uncertainties.

2.3.8 Mode-Matching

As described in the previous sections, the mode spectrum of a resonator consists of the fundamental (Gaussian) mode and higher-order modes (cf. figure 2.12). When light is coupled into the resonator, depending on the properties of the incoming beam and the resonator, either a multitude of modes are excited or just a single
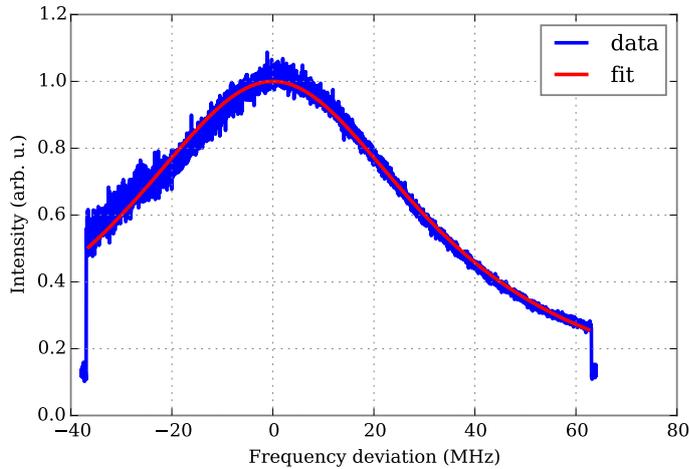
Figure 2.16: Transmission through cavity in dependence of detuning from resonance frequency. Shown are the data (blue) and a Lorentzian fit (red). The data is obtained with a single-photon counting module and already corrected for the change of diffraction efficiency of the AOM.

one. The process of shaping the incoming beam to excite only the desired modes while not coupling to the others is called mode-matching. For the purposes of the cavity used in this report, it is important to achieve good coupling to the fundamental mode while ideally not coupling to other modes at all.

A schematic setup for coupling into the resonator is shown in figure 2.17. The
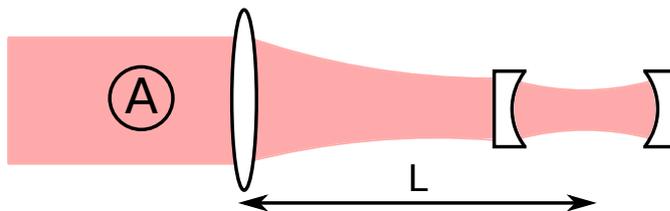
Figure 2.17: Coupling into the resonator is achieved with a lens at distance L from the center of the cavity. It is assumed that the beam before the lens is perfectly collimated.

easiest approach to optimize the coupling, is to first calculate the properties of the fundamental mode of the resonator and then use the ABCD law (cf. section 2.3.2) to propagate the beam out of the resonator and through the coupling lens to position (A), as shown in figure 2.17. This gives the ideal incident beam in dependence of the focal length of the coupling lens and its distance from the

27

resonator. Since the actual incident beam before the lens is known (assumed to be perfectly collimated with known radius[8]), the focal length of the lens and its distance from the cavity have to be adjusted so that the calculated beam at (A) is identical to the actually measured beam.

For spherical mirror resonators with identical mirrors, the waist of the fundamental mode has to be centered between both mirrors. This position is described by $z = 0$ with the beam propagating along the z-axis. The fundamental mode is a Gaussian beam that coincides with itself after one round trip in the resonator. There are two possible approaches of how to calculate this. One can either start with the condition that the wavefront radius of the Gaussian mode must be the same as the radius of curvature of the resonator mirrors at the positions of the mirrors, in order for the beam to retrace itself. Together with the positions of both mirrors, this fixes the parameters of the Gaussian beam for the fundamental mode. Another, simpler approach is to use the ABCD law introduced in equation 2.26, using the fact that the q-parameter (equation 2.20) fully characterizes the Gaussian beam profile. We want the beam to retrace itself, therefore the q-parameter has to be the same after one round-trip ($q_1 = q_2$). This leads to

$$q = \frac{Aq + B}{Cq + D} \tag{2.52}$$

with the ray transfer matrix

$$M = \begin{pmatrix} A & B \\ C & D \end{pmatrix} \tag{2.53}$$

representing one round-trip in the resonator.

This means that for any given position z within the resonator, the q-parameter of the Gaussian beam must be the same when applying the ABCD law with the ray transfer matrix M for one round trip. The calculation simplifies significantly when selecting $z = 0$, because $q(0)$ is entirely imaginary. This is due to the wavefront radius $R(z)$ becoming infinitely large for $z \to 0$. Therefore, the waist of the beam can easily be calculated and from this, one obtains all other parameters.

Let the distance between both mirrors be d and the radius of curvature of the spherical mirrors be R. Starting at $z = 0$, the beam propagates distance $\frac{d}{2}$ in free space characterised by $M_f\left(\frac{d}{2}\right)$, then it is reflected by the second mirror ($M_{r,2}$), propagates back to the first mirror ($M_f(d)$) and is reflected by the first mirror ($M_{r,1}$) before propagating back to $z = 0$ in free space ($M_f\left(\frac{d}{2}\right)$). The final ray

---

[8]The radius is measured at various positions along the beam with a WinCam UCD 23

transfer matrix of one round trip is then (cf. table 2.1)

$$M = \underbrace{\begin{pmatrix} 1 & \frac{d}{2} \\ 0 & 1 \end{pmatrix}}_{M_f\left(\frac{d}{2}\right)} \underbrace{\begin{pmatrix} 1 & 0 \\ \frac{2}{-|R|} & 1 \end{pmatrix}}_{M_{r,1}} \underbrace{\begin{pmatrix} 1 & d \\ 0 & 1 \end{pmatrix}}_{M_f(d)} \underbrace{\begin{pmatrix} 1 & 0 \\ \frac{2}{-|R|} & 1 \end{pmatrix}}_{M_{r,2}} \underbrace{\begin{pmatrix} 1 & \frac{d}{2} \\ 0 & 1 \end{pmatrix}}_{M_f\left(\frac{d}{2}\right)}$$

$$= \begin{pmatrix} 1 - 4\frac{d}{|R|} + 2\frac{d^2}{|R|^2} & 2d - 3\frac{d^2}{|R|} + \frac{d^3}{|R|^2} \\ -4\frac{d}{|R|^2} & 1 - 4\frac{d}{|R|} + 2\frac{d^2}{|R|^2} \end{pmatrix} = \begin{pmatrix} A & B \\ C & D \end{pmatrix}. \tag{2.54}$$

Using this ray transfer matrix with the ABCD law (equation 2.52) and solving for q, we obtain two solutions

$$q = \pm\frac{1}{2}\sqrt{d(-2|R| + d)}. \tag{2.55}$$

Note that q must be imaginary and this leads to the following condition

$$0 \le d \le 2|R|, \tag{2.56}$$

which is the confinement condition for a symmetric resonator [28]. Since $W(z) \in \mathbb{R}$, only the solution with the plus sign is physically meaningful (cf. equation 2.20). From this, we can extract the waist of the mode (using equations 2.20 and 2.22)

$$W(0) = W_0 = \sqrt{\frac{\Im(q)\lambda}{\pi}}, \tag{2.57}$$

and with equation 2.23 the Rayleigh length

$$z_0 = \Im(q). \tag{2.58}$$

$\Im(q)$ means the imaginary part of q.

The coupling of the incident beam into the resonator can be done by using more than one lens, but to keep it simple, the following calculation assumes a perfectly collimated beam with waist W_I before a single thin lens of focal length f. Let the distance between the lens (assumed to have no thickness) and the outer edge of the first mirror of the resonator be L.

When coupling light into the resonator, it first hits the planar outer surface of the first mirror, passes through the medium of the mirror and finally exits on the curved side of the mirror. The mirror can thus be described by a combination of three ray transfer matrices (cf. table 2.1)

$$M_m = \underbrace{\begin{pmatrix} 1 & 0 \\ \frac{n_2 - n_1}{n_1|R|} & \frac{n_2}{n_1} \end{pmatrix}}_{\text{convex surface}} \underbrace{\begin{pmatrix} 1 & b \\ 0 & 1 \end{pmatrix}}_{\text{propagation}} \underbrace{\begin{pmatrix} 1 & 0 \\ 0 & \frac{n_1}{n_2} \end{pmatrix}}_{\text{planar surface}} = \begin{pmatrix} 1 & b\frac{n_1}{n_2} \\ \frac{n_2 - n_1}{|R|n_1} & b\frac{n_2 - n_1}{|R|n_2} + 1 \end{pmatrix}, \tag{2.59}$$

where $n_1 \approx 1$ is the refractive index of air, n_2 the refractive index of the mirror's material and b the thickness of the mirror (assuming that the effects of the curvature are negligible with respect to the thickness).

The ray transfer matrix for the whole path of the incident beam then becomes

$$M = \begin{pmatrix} 1 & \frac{d}{2} \\ 0 & 1 \end{pmatrix} \begin{pmatrix} 1 & b\frac{n_1}{n_2} \\ \frac{n_2-n_1}{|R|n_1} & b\frac{n_2-n_1}{|R|n_2}+1 \end{pmatrix} \begin{pmatrix} 1 & L \\ 0 & 1 \end{pmatrix} \begin{pmatrix} 1 & 0 \\ -\frac{1}{f} & 1 \end{pmatrix} = \begin{pmatrix} A & B \\ C & D \end{pmatrix} . \tag{2.60}$$

Using the ABCD law (equation 2.26) with this matrix leads to

$$\frac{A(L,f)q_0 + B(L,f)}{C(L,f)q_0 + D(L,f)} - q_1 = 0 , \tag{2.61}$$

where q_0 is the q-parameter before the incoupling lens and q_1 is the q-parameter at the center of the resonator. Since we want ideal coupling to the fundamental mode, it has to be $q_1 = q$ (with q from equation 2.55). Furthermore, we assume that the beam is perfectly collimated before the coupling lens and thus $q_0 = i\frac{\pi W_I^2}{\lambda}$ with W_I being the beam radius before the lens.

Solving equation 2.61 for distance L yields the optimal distance of the incoupling lens from the center of the resonator, in dependence of focal length f (all other parameters are fixed by the resonator design). Since equation 2.61 has two free parameters (f, L), there are an infinite number of possible solutions. However, for a solution to physically make sense, both parameters must be real. With this constraint, only one solution remains which gives both, the ideal focal length of the lens as well as its ideal distance from the resonator. In practice, this solution was found by numerically minimizing the imaginary part of $L(f)$.

Note that the coupling to the fundamental mode is very sensitive to radial misalignment of the beam. Ideally, it would pass through the center of both cavity mirrors and deviations of about $50\,\mu m$ result in only half the coupling efficiency (the beam waist at the center of the cavity is $62\,\mu m$). This is visualized in figure 2.18.

2.3.9 Suppression of Off-Resonant Frequencies

The suppression of off-resonant frequencies depends on the finesse of the cavity and its detuning from resonance with respect to the FSR (cf. equation 2.36). As mentioned earlier, best suppression is achieved for detunings of half the FSR. This gives a suppression factor of

$$\chi = \frac{1}{1 + \left(\frac{2\mathcal{F}}{\pi}\right)^2} , \tag{2.62}$$
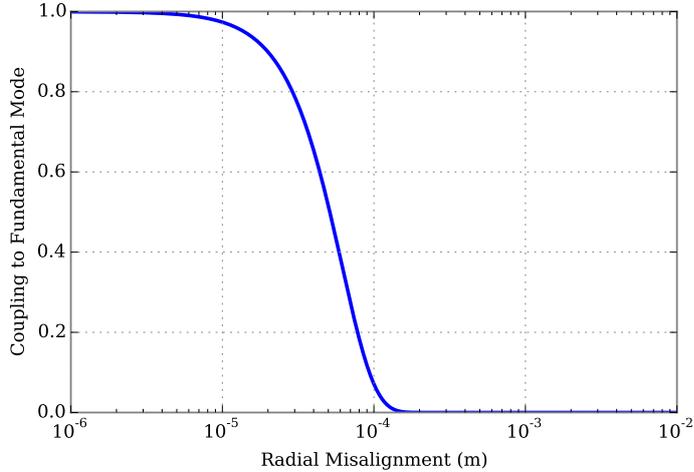
Figure 2.18: Change of coupling efficiency to fundamental mode with radial misalignment of the beam. The misalignment is assumed to be in such a way that the beam is always parallel to the optical axis. This calculation is based on a focal lens of $175\,\mathrm{mm}$ placed $174\,\mathrm{mm}$ before the center of the cavity.

where $I = \chi I_{\mathrm{max}}$ and I_{max} is the on-resonance transmitted intensity. With the finesse determined for this cavity (cf. section 2.3.7), χ becomes

$$\chi_{\mathrm{theoret.}} = (-43.04 \pm 0.04)\,\mathrm{dB}\,. \tag{2.63}$$

Figure 2.19 shows the suppression over the whole range of one FSR. This data was recorded early in the optimization process and shows significant coupling to transverse modes. However, the maximal suppression still reaches almost $-40\,\mathrm{dB}$ but not at half the FSR. The coupling to the fundamental mode has since been improved, which also reduced the intensities of the transverse modes.

Since it is a requirement for the cavity to be fiber-coupled (cf. section 2.1.3), transverse modes are suppressed even more by optimizing the coupling of the fundamental mode of the cavity to the fiber. This is shown in figure 2.20, where no transversal modes can be seen any more. Fitting the peaks with Lorentzians and extracting the value of maximal suppression yields

$$\chi_{\mathrm{exp.}} = -42.7\,\mathrm{dB}\,, \tag{2.64}$$

which is close to the theoretical value.
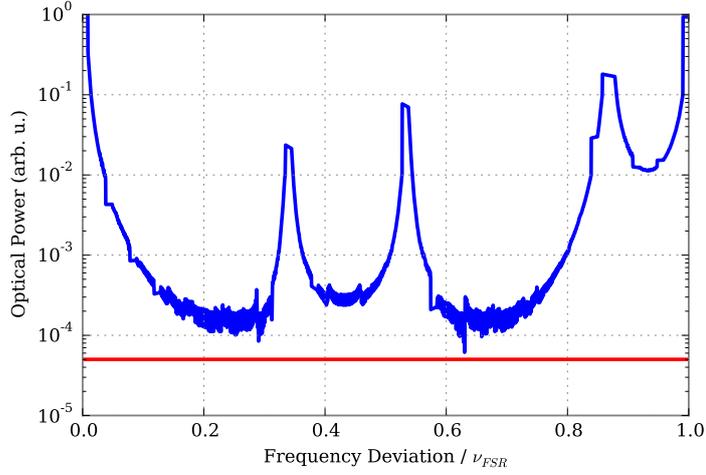
Figure 2.19: Measured optical power behind the cavity while scanning over one FSR. The x-axis shows the deviation from the fundamental mode. 3 transverse modes can be seen. This measurement is taken directly after the cavity. Note that the resolution is not very high and thus some "edgy" parts can be seen. Note also that this is early data and the coupling to the fundamental mode has since been improved (see text).

2.3.10 Suppression of Fiber Background

Before reaching the cavity, the light from the nanofiber is filtered by a volume Bragg grating[9]. It has a linewidth of 0.12 nm around a wavelength of 852 nm and its spectral response can be modeled by a Gaussian. To determine the suppression of background light from the nanofiber, two measurements, one with cavity in place and one without cavity are performed and their results compared. To account for typical background light, the blue trap laser (783 nm) of the main experiment is sent into the nanofiber. While it will be blocked by the Bragg grating, fluorescence and Raman scattered light will reach the cavity. It is assumed that over this small wavelength interval, the intensity of the background is constant[10]. A schematic of this setup is shown in figure 2.21.

Let $\tilde{P}(\nu)$ be the power per unit of frequency. The power in interval $\nu_0 \leq \nu \leq \nu_1$ would then be $P(\nu_0, \nu_1) = \int_{\nu_0}^{\nu_1} \tilde{P}(\nu) \mathrm{d}\nu$. After passing the Bragg grating, the spectral shape of the background is that of a Gaussian with a width of 0.12 nm,

---

[9]Optigrate RBG-852-94

[10]In earlier experiments with background light from fibers, this was found to be true

32
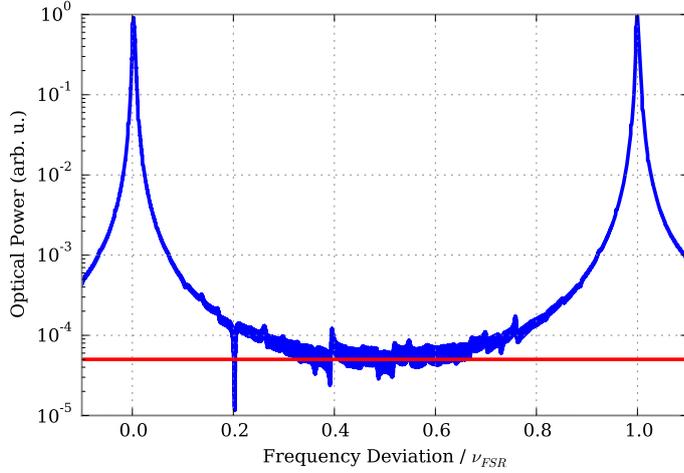
Figure 2.20: Transmitted intensity while scanning over one FSR. The peaks of the fundamental mode are at 0 and 1 and in-between no significant coupling to any transverse modes can be seen. This measurement is taken by coupling the light that exits the cavity into a single-mode fiber and measuring after the fiber. The red horizontal line indicates the calculated maximal suppression of $-43.04\,\mathrm{dB}$.

thus

$$\tilde{P}_{\mathrm{VBG}}(\nu) = \tilde{P}_0 e^{-\frac{\nu^2}{2\sigma^2}} \,. \tag{2.65}$$

with $\sigma = 20.38\,\mathrm{GHz}$[11].

When bypassing the cavity but maintaining the single-mode fiber, the light is attenuated by η_0 and then detected. This leads to

$$P_{\mathrm{nocav}} = \eta_0 \int_0^\infty \tilde{P}_{\mathrm{VBG}}(\nu)\mathrm{d}\nu \,, \tag{2.66}$$

where P_{nocav} is the total detected power. If the cavity is put in place, the light is attenuated by a different factor η_{cav} and off-resonant frequencies are suppressed as shown in figure 2.4. This yields

$$P_{\mathrm{cav}} = \eta_{\mathrm{cav}} \int_0^\infty \tilde{P}_{\mathrm{VBG}}(\nu)\xi_{\mathrm{cav}}(\nu)\mathrm{d}\nu \,, \tag{2.67}$$

where $\xi_{\mathrm{cav}}(\nu) = \int_A \frac{I_{\mathrm{cav}}(\nu)}{I_0}\mathrm{d}A$ is the normalized transmission through the cavity and $I_{\mathrm{cav}}(\nu)$ is given by equation 2.36.

---

[11]Value taken from a fit to the graph provided in the datasheet.
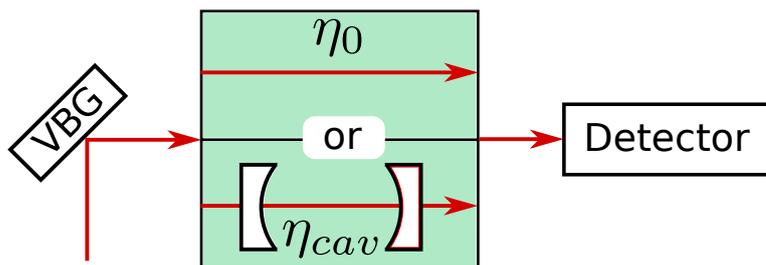
Figure 2.21: Schematic setup for measurement of background suppression. The beam is filtered by a volume Bragg grating before either being directly routed to the detector or filtered by the cavity before detection. η_0 and η_cav are the factors introduced in equations 2.66 and 2.67.

Comparing both results gives

$$\frac{P_\text{cav}}{P_\text{nocav}} = \frac{\eta_\text{cav}}{\eta_0} \frac{\int_0^\infty \tilde{P}_\text{VBG}(\nu)\xi_\text{cav}(\nu)\mathrm{d}\nu}{\int_0^\infty \tilde{P}_\text{VBG}(\nu)\mathrm{d}\nu} \, . \tag{2.68}$$

This can not be solved analytically. Using the values for the cavity as determined above, this fraction becomes 0.0024 when using $\frac{\eta_\text{cav}}{\eta_0} = 0.39$ as experimentally determined. However, the experimental result is 0.015 ± 0.007. These are significantly different and it is still unclear why. The dark counts of the detector have been considered and also the fact that the maximal suppression is less than calculated can not account for this discrepancy.

2.3.11 On-Resonance Transmission

The on-resonance transmission is $\frac{P_\text{out}}{P_\text{in}}$, where P_out is the transmitted optical power, measured directly after the cavity, and P_in is the power before the resonator. This highly depends on the position of the coupling lens, the orientations of the coupling mirrors and the cleanness of the cavity mirrors. Since one cavity mirror is mounted on a translation stage, its position also affects the coupling efficiency. All these variables might change whenever the setup is adjusted. Therefore, only the highest achieved transmission is given here.

With the current setup, it is impossible to stabilize the cavity while at the same time measuring the power, as this effectively blocks the beam path. To nevertheless measure the on-resonance transmission, the cavity is scanned while measuring the intensity after the cavity. Scanning the cavity refers to varying the distance between both mirrors with the piezo crystal (cf. section 2.2), which leads to the recording of transmission peaks. Then, Lorentzians are fitted to these peaks and the mean of their maxima divided by the mean power measured before the

cavity gives the transmission. The highest measured transmission is

$$T = (76.6 \pm 0.7)\,\% \tag{2.69}$$

2.4 Resonator Losses

In the previous section, we have derived an equation for the intensity within the resonator (equation 2.36). While this equation is well-suited for a qualitative investigation of the properties of the resonator, it does not provide the intensity after the resonator when continuously coupling light into it. To account for the continuous incoupling of light, the equation for the complex amplitude needs to be of the following shape (cf. 2.19)

$$E_n(t) = \alpha e^{-i\phi} E_{n-1}(t - \tau) + t_1 E_0(t)\,, \tag{2.70}$$

where t_1 is the amplitude transmission of the incoupling mirror and τ is the time per round-trip. Index n designates the n-th round-trip within the resonator. Subtracting $E_{n-1}(t)$ on both sides gives the change of amplitude during one round trip.

$$E_n(t) - E_{n-1}(t - \tau) = \left(\alpha e^{-i\phi} - 1 \right) E_{n-1}(t - \tau) + t_1 E_0(t)\,. \tag{2.71}$$

In the stationary case, this difference is 0 and $E_{n-1}(t - \tau) = E_n(t) =: E(t)$ and thus

$$E(t) = \frac{t_1 E_0(t)}{1 - \alpha e^{-i\phi}}\,. \tag{2.72}$$

This is similar to equation 2.34 and thus, analogously to above, leads to the result

$$I = \frac{\tilde{I}_{\max}}{1 + \left(\frac{2\mathcal{F}}{\pi} \right)^2 \sin^2 \left(\frac{\pi\nu}{\nu_{\mathrm{FSR}}} - \Delta\zeta \right)} \tag{2.73}$$

with $\tilde{I}_{\max} = \frac{T_1 I_{\mathrm{in}}}{\beta^2}$. Here, $T_i = t_i^2$ is the intensity transmission with index 1 for the first (incoupling) mirror and 2 for the second (outcoupling) mirror. The result is very similar to before with just the maximal intensity $\tilde{I}_{\max}$ being different. The intensity after the cavity is $T_2 I \left(1 - \frac{\mathcal{L}}{2} \right)$ with the intensity losses $\mathcal{L}$ per round-trip ($\frac{\mathcal{L}}{2} + T_i + R_i = 1$). Note that α is not simply $1 - \mathcal{L}$ but comprises the attenuation due to losses (medium and non-ideal mirrors) as well as the attenuation resulting from $r_i < 1$ with r_i being the amplitude reflection coefficient of mirror i.

The intensity behind the cavity can also be approximately expressed by the Lorentzian [32]

$$I_{\mathrm{out}} \approx \frac{4 T_1 T_2}{(\mathcal{L} + T_1 + T_2)^2 + 4(\Delta\phi)^2} I_{\mathrm{in}}\,, \tag{2.74}$$

with $\Delta\phi = \frac{\pi\nu}{\nu_{\text{FSR}}} - \Delta\zeta$. Note that equation 2.74 is an approximation for T_1, T_2, $\mathcal{L}$, $\Delta\phi \ll 1$. A calculation of the transmitted power with increasing losses is shown in figure 2.22. The finesse $\mathcal{F}$ then becomes [32]

$$\mathcal{F} \approx \frac{2\pi}{\mathcal{L} + T_1 + T_2}. \tag{2.75}$$

Note that the on-resonance reflected intensity is given by [32]

$$I_{\text{refl}} = \frac{(\mathcal{L} - T_1 + T_2)^2}{(\mathcal{L} + T_1 + T_2)^2} I_{\text{in}}. \tag{2.76}$$
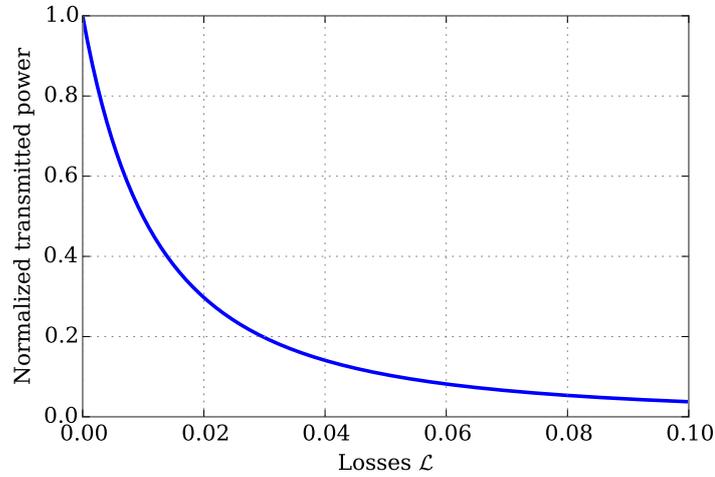
Figure 2.22: Change of transmitted power on resonance ($\Delta\phi = 0$) when increasing the losses within the resonator. These losses comprise losses due to the medium as well as losses during reflection or transmission at the mirrors. Basis for this graph is equation 2.74 with $T_1 \approx T_2 \approx 0.012$, as for the cavity used in this report.

2.4.1 Estimating Losses in the Cavity

With equation 2.75, the losses inside the cavity can be estimated with known transmissions of the mirrors and the finesse

$$\mathcal{L} = \frac{2\pi}{\mathcal{F}} - T_1 - T_2. \tag{2.77}$$

The transmissions of the mirrors are measured as $T_1 = (1.30 \pm 0.09)\%$ and $T_2 = (1.20 \pm 0.04)\%$ and the finesse is calculated in section 2.3.7 and is $\mathcal{F} = 223 \pm 1$.

This gives $\mathcal{L} = (0.3 \pm 0.1)\,\%$. Note that $\mathcal{L}$ are the losses per round trip in the resonator. The average number of round trips can be calculated using equation 2.46 and is

$$N_{\text{RT}} = 35.49 \pm 0.16\,.$$ (2.78)

With this, we can estimate the total losses inside the resonator to be

$$\mathcal{L}_{\text{total}} = \mathcal{L}N_{\text{RT}} = 1 - \frac{(T_1 + T_2)\mathcal{F}}{2\pi} = (12.9 \pm 3.5)\,\%\,.$$ (2.79)

The measured maximal transmission of the fundamental mode is $(76.6 \pm 0.7)\,\%$ (cf. equation 2.69) and the expected on-resonance reflection with the losses estimated above is $(2.7 \pm 0.9)\,\%$ (cf. equation 2.76). The sum of all these effects gives $(92 \pm 4)\,\%$. There are about $8\,\%$ missing. This is an indication that there is still coupling to transverse modes. Furthermore, the transmission of the cavity mirrors was measured at the very beginning, before placing them in the cavity. Due to dust or non-ideal cleaning, the values for T_1 and T_2 might be less now, which leads to an underestimation of the losses (cf. equation 2.79).

2.5 Experimental Setup

In this section, the experimental setup of the cavity filter is described. A sketch of the setup is shown in figure 2.23. Two beams are coupled into the cavity. A reference laser, operating at $780\,\text{nm}$ and a probe beam ($852\,\text{nm}$), which comes directly from the experiment.

The reference laser is used to generate an error signal to provide feedback to the piezo-actuator of the cavity. This allows for stabilization of the distance between the cavity mirrors and is described in more detail in section 2.7. To characterize the cavity, a laser running at $852\,\text{nm}$ is sent through the fiber at point (1) in figure 2.23. Both lasers are described in section 2.6.2.

The probe light arrives in a polarization maintaining fiber. Its linear polarization is then adjusted with a half-wave plate to maximize transmission through the optical isolator[12]. The optical isolator is important to protect the experiment from light reflected at the cavity. In particular, in EIT experiments the cavity reflects almost all of the control beam. The probe beam is then joined with the beam of the reference laser by reflection on a shortpass filter[13]. The reference laser passes two mirrors before it is joined with the probe beam. Its coupling to the cavity can thus be changed without affecting the coupling of the probe. Then, both beams are focused with a lens[14] that is mounted on a translation stage and

---

[12]Thorlabs NIR Freespace Tandem Isolator (IOT-5-850-VLP)
[13]Thorlabs DMSP805
[14]Thorlabs LA1229-B
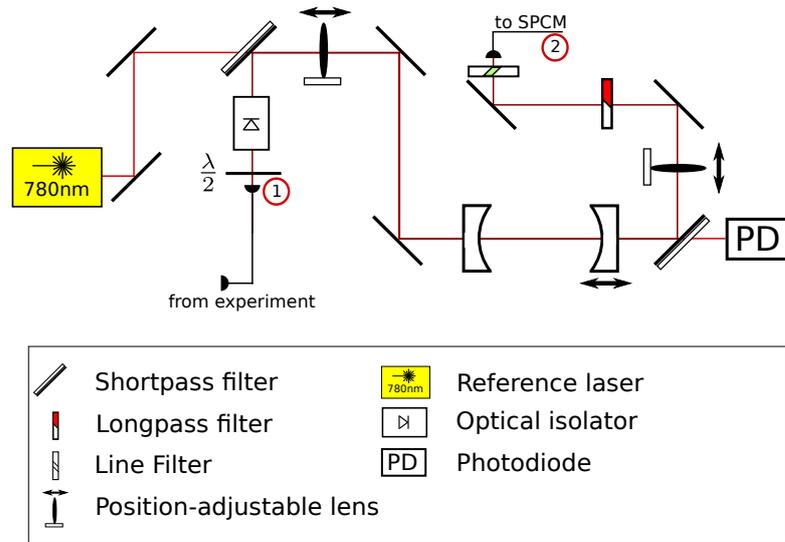
Figure 2.23: Experimental Setup of the Cavity Filter. The reference laser is shown in yellow and includes the saturation spectroscopy setup for its stabilization (cf. section 2.6.2). "PD" signifies a photodiode and "SPCM" a single-photon counting module. The arrows next to the lenses and the second cavity mirror indicate their mounting on translation stages.

coupled into the cavity by two mirrors. The lens has a focal length of 175 mm and must ideally be placed 174 mm before the center of the cavity. Theoretically, a maximal coupling to the fundamental mode of 99.97 % can be achieved with this configuration (see section 2.3.8).

Behind the cavity, another shortpass filter separates the reference beam from the probe beam. While the reference beam is measured by a photodiode[15], the probe beam passes another lens, identical to the one before the cavity, and is coupled into a single-mode fiber by two mirrors. The reference beam is has a larger power than the probe beam and a small fraction of it is reflected by the shortpass filter. To ensure that only a negligible amount of the reference beam is coupled into the fiber, a longpass[16] and a laser line[17] filter are placed before the fiber coupler. The distance of the second lens from the cavity is chosen the same like for the first lens. Since the beam before the first lens is very well collimated, this—due to symmetry reasons—then results in a well-collimated beam behind the second lens.

The overall transmission of probe light through the whole setup is 44 % (between

---

[15]Custom-built. Amplified with an operational amplifier. Characteristics shown in figure 2.24.
[16]Asahi XIL 0840
[17]Semrock MaxLine LL01-852-12.5

points (1) and (2) in figure 2.23), transmission through the optical isolator is 85 % and the coupling efficiency to the fiber at point (2) is 88 %.

The photodiode used for stabilization of the cavity, marked "PD" in figure 2.23, is amplified by an operational amplifier and shows linear behaviour within a range of 0 µW to 80 µW, where it saturates. This is shown in figure 2.24.
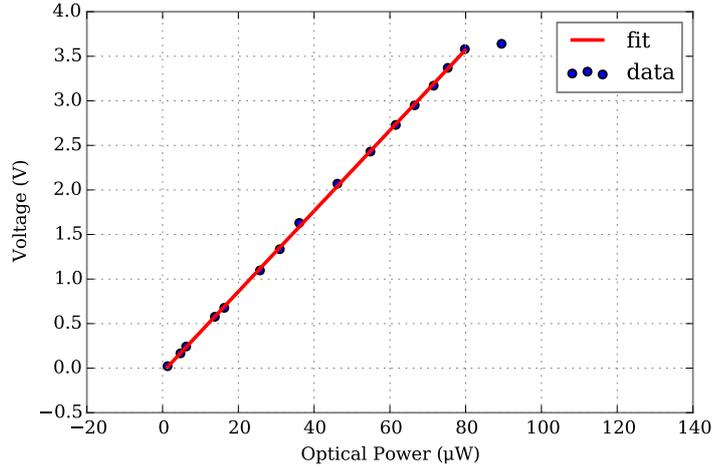
Figure 2.24: Power-Voltage characteristics of the photodiode. Saturation occurs at around 80 µW. The slope of the fit is $(4.52 \pm 0.02) \times 10^{-2}\,\mu\text{W V}^{-1}$

The reflection of the shortpass filter that separates probe and reference beam after the cavity depends highly on its angle with respect to the incoming beam. Best reflection is obtained for angles close to 45°. The reflection of the probe beam is then 99 % and for the reference laser it is 8 %.

2.6 Laser Stabilization

Since the cavity is stabilized to a reference laser (cf. section 2.7), it is important for the reference laser to be frequency-stabilized. To allow for an accurate characterization of the cavity, the probe laser, too, needs to be frequency-stabilized. This is achieved with saturation spectroscopy and is described in section 2.6.1. The setup of the lasers is then discussed in section 2.6.2.

2.6.1 Saturation Spectroscopy

Saturation spectroscopy can be used to resolve the hyperfine atomic structure that would otherwise be invisible due to Doppler broadening. In absorption spectroscopy, a laser beam is sent through a gas cell and then detected by a photodiode.

Depending on with which element the gas cell is filled, scanning the frequency of the laser leads to a change in the detected intensity at the photodiode. One observes absorption peaks at frequencies close to atomic transitions. These result from atoms scattering the light out of the beam path. However, since the atoms are moving at different speeds, they "see" the frequency of the light Doppler-shifted to red when they move with the beam and to blue when moving in opposite direction of the beam. This means that a light field, which is slightly off-resonance with respect to this transition, is still on-resonance to some atoms that are moving in a way that the frequency of the light is Doppler-shifted to match the transition frequency.

The basic idea of saturation spectroscopy is to have two beams of exactly the same frequency spatially coinciding but propagating in opposite directions. One beam, usually of stronger intensity, is called pump beam and the other is called probe beam. The probe beam is measured while scanning the frequencies of both beams simultaneously over the transition frequency. An easy way to achieve this, is to either split one laser beam into two separate beams or to place a mirror behind the gas cell that reflects the beam back through the cell.

Atoms moving in direction of one beam will see it red-shifted and the opposing beam blue-shifted. This means that, while scanning the laser, if one beam is resonant with the transition, the other one is not. Therefore, absorption occurs in both beams. However, atoms that do not move in direction of either beam, see both beams on-resonance with the transition at the same time, because there is no Doppler-shift involved. In this case, the pump beam can *saturate* the absorption, which results in the probe beam being much less absorbed. In the transmission spectrum of the probe, this shows up as a peak, a so-called lamb dip. The spectral position of the lamb dip corresponds to the frequency of the atomic transition. With this method, it is possible to resolve the hyperfine structure of a transition.

In the special case where the laser frequency is exactly in the middle of two transitions with the same ground state and their frequency difference is small compared to the Doppler width, one also observes these peaks. This is because atoms moving in direction of the pump see it red-shifted to one transition, while they see the probe blue-shifted to the other transition. The pump can then saturate one transition, depopulating the ground state significantly. The absorption of the probe is then much reduced since it can only excite atoms that are in the ground state. These peaks are called crossover peaks. The same is true for transitions with distinct ground states but a shared excited state. The pump saturates one transition but the decay from the excited state can now happen to either ground state. The result is that the probe beam is less absorbed because some of the atoms are in the other ground state, which it can not excite.

Figure 2.25 shows the spectrum of Rubidium for saturation spectroscopy. If
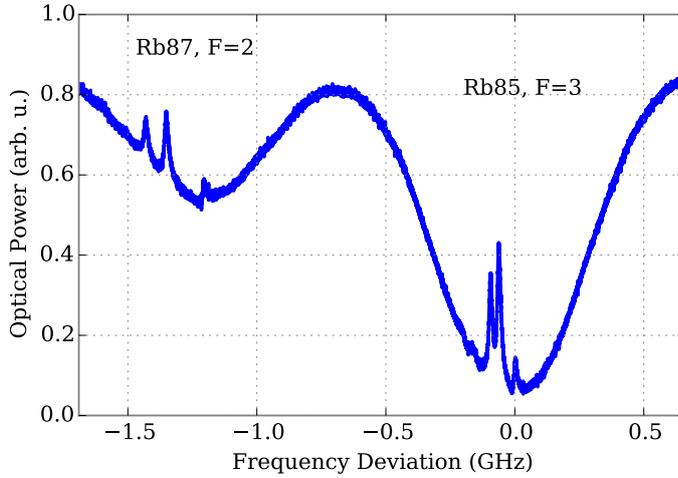
Figure 2.25: Saturation spectroscopy using a gas cell with Rubidium 87 and Rubidium 85. The x-axis shows the frequency deviation from the Rubidium 85 D2 $F = 3 \rightarrow F' = 4$ transition. The labels $F = 2$ and $F = 3$ refer to the ground state of the transitions.

correcting for the absorption slope by fitting and subtracting a Gaussian, the lamb dips can be seen much better. This is shown in figure 2.26.

2.6.2 Locking the Laser

There are two lasers used in the setup. The probe laser, which is used to simulate light coming from the experiment and allowing for a characterization of the resonator and the reference laser that is needed to lock the cavity to a constant FSR (see section 2.7). Both, the reference and the probe laser are external-cavity diode lasers (ECDL) in a littrow configuration [33] (see figure 2.27). The diode emits light which is collimated with a lens before reaching a Bragg grating. The grating diffracts the 1st order beam back into the diode and thus acts as the second mirror of the laser cavity, stabilizing the wavelength to cavity modes depending on its distance from the diode. This distance, together with the diffraction angle, can be adjusted by tilting the grating with a micrometer screw and a piezo crystal. The 0th order diffracted beam is reflected out of the system and corresponds to the beam emitted by the laser in figures 2.28a and 2.28b.
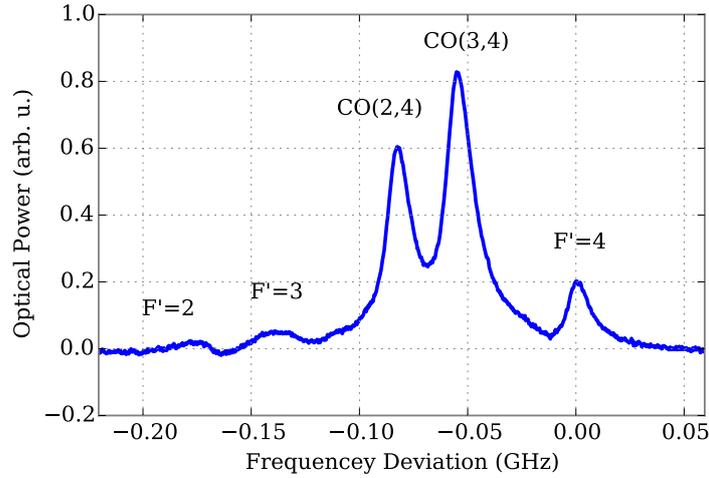
Figure 2.26: Saturation spectroscopy of Rubidium 85. Shown are the hyperfine transitions $F = 3 \rightarrow F'$. This corresponds to to the transitions shown in figure 2.25 when correcting for the Doppler-broadened background. CO(3,4) means the crossover peak of transitions $F = 3 \rightarrow F' = 3$ and $F = 3 \rightarrow F' = 4$. The x-axis shows the frequency deviation from the Rubidium 85 D2 $F = 3 \rightarrow F' = 4$ transition.

Reference Laser

The reference laser is tuned to a wavelength of 780.241 nm (Rubidium D2 line [34, 35]). Note that it is not important to which exact hyperfine transition this laser is locked. In fact, the possibility to use any of the D2 transitions of both, Rubidium 87 and Rubidium 85, facilitates the stabilization of the cavity (cf. section 2.7).

The optical setup of the laser is shown in figure 2.28a. First, the laser passes a prism pair to reshape it to have a circular beam profile. An optical isolator[18] prevents backreflection into the diode, which might lead to mode-jumps of the laser. The beam is then partially reflected by a beamsplitter which transmits 90 % and reflects 10 %. The transmitted part passes a half-wave plate followed by a polarizing beamsplitter cube to adjust the power of the reference beam and is then coupled into the cavity (cf. figure 2.23).

The fraction of the beam being reflected at the 90:10 beamsplitter also passes a half-wave plate followed by a polarizing beamsplitter cube (PBC) to adjust the intensity. It then propagates through a gas cell containing both Rubidum 85 and Rubidum 87. It is then reflected by a mirror and passes a quarter-wave plate twice, which is identical to passing a half-wave plate once, where the polarization

---

[18]Thorlabs IO-5-NIR-LP
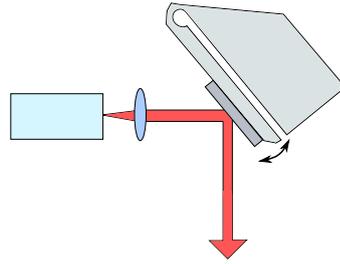
Figure 2.27: Littrow configuration for an ECDL. The angle and position of the Bragg grating (dark gray) can be adjusted with a micrometer screw and a piezo-electric actuator (not shown).

(a) Reference laser   (b) Probe laser.
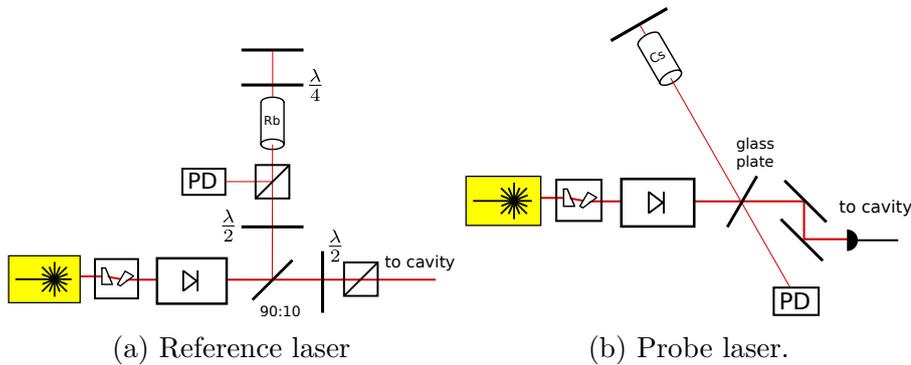
Figure 2.28: Laser setup with saturation spectroscopy.

direction is changed to be reflected at the PBC instead of transmitted. Finally, the beam is detected by a photodiode. The beam propagating through the rubidium cell before reflection corresponds to the pump beam above. After reflection, passing the cell a second time, it is termed probe beam. The photodiode then records a spectrum similar to the one shown in figure 2.25 when scanning the laser frequency.

With a PI controller, the laser can be locked to a flank of one of these peaks.

Probe Laser

The probe laser is operated at a wavelength of 852.347 nm (Cesium D2 line [26]). Similar to the reference laser, it passes a prism pair to ensure a circular beam cross-section and an optical isolator[19] to protect the diode and prevent mode-jumps (see figure 2.28b). The main part of the beam is then coupled into a fiber that is connected with the cavity setup (cf. figure 2.23). A fraction of the beam is reflected by a glass plate and sent through a cesium cell for saturation spectroscopy.

---

[19]Thorlabs NIR Freespace Tandem Isolator (IOT-5-850-VLP)

2.7 Cavity Stabilization

The cavity is actively stabilized to a reference laser for constant transmission of the probe light, as well as constant suppression of the control field and the fiber background. While the probe beam is coupled to the fundamental mode, this is not true for the reference laser. Its coupling is purposely misaligned to couple to many modes. The stabilization of the cavity essentially means a stabilization of the FSR and thus of the piezo-controlled position of the second mirror. This is done by using a PI controller to lock the cavity to one of the transmission peaks of the reference beam. To maximize the transmission of the probe, this peak needs to spectrally overlap with the peak of the probe beam. An ideal case is shown in figure 2.29. Locking to the rising flank of the reference beam maximizes the
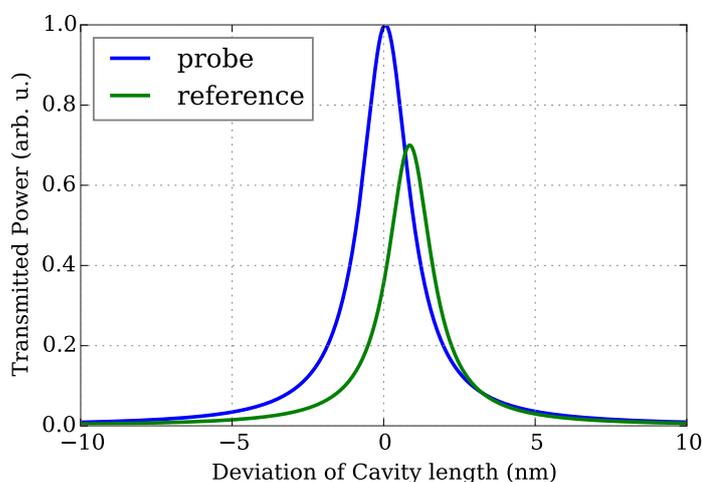
Figure 2.29: Ideal FSR for alignment of probe and reference laser transmission peaks. Shown are the transmitted powers of the probe and reference laser with changing distance between both mirrors of the cavity. The x-axis corresponds to the positional change of the second cavity mirror from a point at which the probe transmission is maximized.

transmission of the probe beam while additionally optimizing the sensitivity of the lock by locking to the steepest slope. Such an overlap can be realized by varying the FSR with the translation stage and the piezo.

It should be noted that the translation stage expands perpendicular to the axis of motion when increasing the distance between the mirrors. Since it is mounted within a slide rail, this can lead to jamming the stage in the slide rail and a deadlock of the piezo crystal. In such a case, the scan range of the piezo is drastically limited and it might very well be that no transmission peak of the probe beam can be

found within the scan interval of the piezo crystal. Therefore, the range of possible adjustments with the micrometer screw is limited to about half a millimetre.

The result of a longterm stability measurement is shown in figure 2.30. Over a
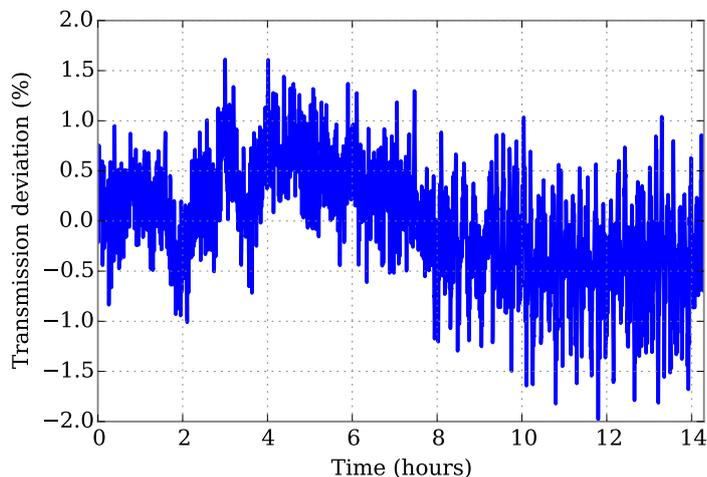
Figure 2.30: Long-term stability of the cavity transmission. Shown is the deviation from the mean value in percent.

time interval of about 14 hours, the transmission only deviates by less than $\pm 1\,\%$. The setup for this measurement is shown in figure 2.31.

The short-term performance is shown in figure 2.32. For this measurement, there is no data on the actual transmission available, only a measurement of the power after the cavity. This means that there could still be effects like small fluctuations in the fiber coupling efficiency that lead to variations of the probe's power before the cavity but they are assumed to be negligible. The deviations of the power behind the cavity are again within about $\pm 1\,\%$.

Note that there were initially major issues with stabilizing the cavity and large fluctuations of transmitted intensity. Fourier transforms showed strong oscillations at frequencies of $35\,\mathrm{Hz}$ and $400\,\mathrm{Hz}$. The reason for this were vibrations transferred to the cavity via the cable for the piezo actuator. Changing the cable to a very flexible one that is additionally fixed to the optical breadboard finally solved this issue.
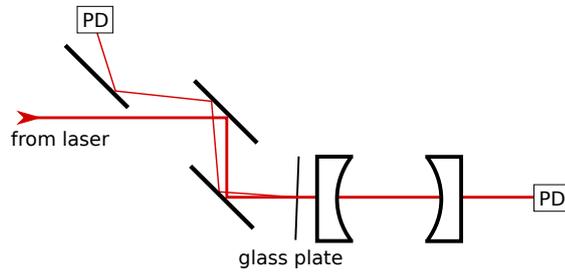
Figure 2.31: Schematic setup for transmission measurement. A glass plate is placed in front of the cavity at almost a right angle to least influence the coupling to the cavity. The reflection of the glass plate is then routed to a photodiode to measure the intensity changes before the cavity. Note that not the real intensity but only its relative changes are of interest for this measurement. The intensity after the cavity is measured with another photodiode.
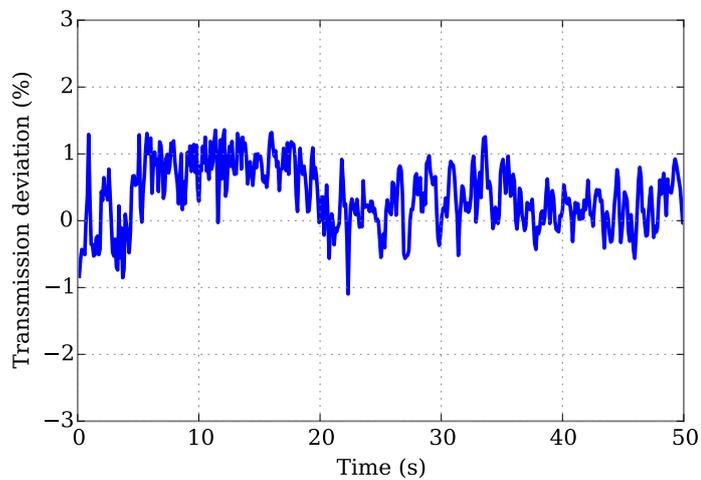
Figure 2.32: Short-term stability of the intensity after the cavity. Shown is the deviation from the mean of all data in percent. Note that this is not a zoom of the data shown in 2.29 but is a different measurement.

2.8 Conclusion

In this chapter, the design, setup and characterization of an FPI that is actively stabilized to a reference laser was discussed. The purpose of this cavity was to filter background light from the fiber, caused by Raman scattering and fluorescence, and to suppress the control field in EIT experiments. These requirements are well-fulfilled, in particular a suppression of $-42.7\,\mathrm{dB}$ of the control field could be achieved and the fiber background is reduced by about $99\,\%$. Thus, the cavity offers good filtering properties for EIT experiments and also for the atom-counting discussed in chapter 3. The transmission of the probe field through the whole setup, including the fiber-coupling before and after the cavity, is $44\,\%$. This transmission is very stable—even on time scales of more than $10\,\mathrm{h}$, where variation of less than $\pm 1\,\%$ have been measured.

The performance of the cavity could potentially be further improved by using mirrors with higher reflectivity. This would result in a higher finesse, which can drastically improve the suppression of both the control field as well as the fiber background. However, this would also increase the average number of round trips inside the resonator and could result in higher losses.

The main problem that occurred during the setup of the cavity were issues concerning its stabilization to the reference laser. There were perturbing vibrations at frequencies of $35\,\mathrm{Hz}$ and $400\,\mathrm{Hz}$. These were transferred to the cavity via the cord connected to the piezo actuator. This was solved by exchanging this cord for a very flexible one that is additionally fixed to the optical breadboard.

Finally, I would like to outline two modifications that would improve the usability of the cavity. As discussed in section 2.7, the translation stage, on which one of the cavity mirrors is mounted, does extent perpendicular to its axis of motion when the distance between the mirrors is adjusted with the micrometer screw. Since the cavity is mounted in a slide-rail, this jams the movement of the mirror and hinders the search for a good locking point. This behaviour of the translation stage was not known before and it is not crucial to the operation of the cavity. Nevertheless, the handling would be much improved if this jamming could be prevented. If at some point a similar cavity is built, one could take this into account when choosing a translation stage. Another possible improvement of the usability would be the modification of the mirror mounts of the cavity. Currently, the mirrors are fixed inside their mounts with a metal strip clamping them in place. While this setup is stable and reliable, it takes some practice to place the mirrors in their mounts. Furthermore, both cavity mounts have to be taken out of the slide rail to do this. It is not possible to place the mounts back in the rail without having to repeat the process of coupling to the fundamental mode. Since this takes quite a bit of time, the cleaning of the cavity mirrors becomes a very lengthy process. This could be facilitated by changing the mounts to fix the mirrors with screws. One could drill

a hole from the top and use screws similar to those used in the commercial mirror mounts.

3 Counting of Atoms Trapped Along a Nanofiber

In this chapter, the counting of atoms in a nanofiber-based trap is discussed. In particular, it is assessed how precisely this can be done with the existing setup of the nanofiber trap and the cavity of chapter 2. A brief introduction to trapping atoms along a nanofiber and the current experimental setup is given in section 3.1. Then, the scattering of light on these atoms and the resulting heating effects as well as possible methods of counter-acting that heating with cooling are described in section 3.2. Finally, different methods to infer the atom number from the experimental data are introduced in section 3.3 and their performance is evaluated with simulated datasets. A conclusion is given in section 3.4.

3.1 Nanofiber-based Atom Trap

As mentioned in chapter 1, nanofibers have a pronounced evanescent field, through which atoms can strongly interact with fiber-guided modes. This interaction can be used to trap atoms in close proximity around the nanofiber by means of an optical dipole trap [5, 14]. The basis for such a trap is the dipole force acting on atoms when irradiating them with far-detuned light with respect to an optical transition [36, 37, 38, 39, 40]. Such a force can be described by a dipole potential [36]

$$U_{\mathrm{dip}}(\vec{r}) = \frac{3\pi c^2}{2\omega_0^3} \frac{\gamma}{\Delta} I(\vec{r})\,, \tag{3.1}$$

where ω_0 is the transition frequency, $\Delta = \omega - \omega_0$ is the detuning, γ is the spontaneous decay rate, and $I(\vec{r})$ is the field intensity. When the frequency of the light is below the transition frequency ($\Delta < 0$), the dipole potential is negative and exerts a force attracting the atom towards higher intensities. Such a light field is termed red-detuned. The opposite is true for higher frequencies, where the atom is pushed to regions of lower field intensity. The light is then called blue-detuned.

In our group, cesium atoms are trapped around a nanofiber by using far-detuned light with respect to the D line transitions[1]. The experimental setup is shown in

---

[1] The D1 line is at $894\,\mathrm{nm}$, the D2 line at $852\,\mathrm{nm}$ and the wavelengths of the trapping lasers are given in figure 3.1.
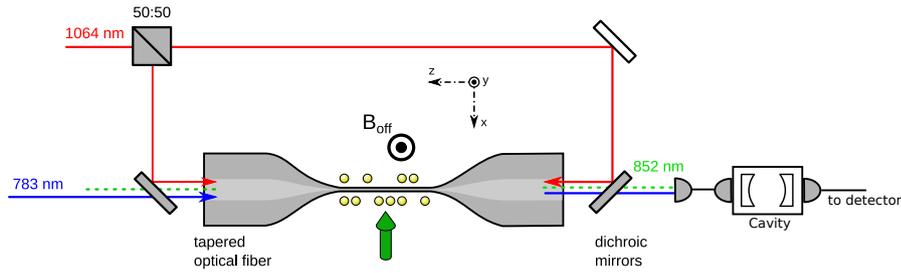
Figure 3.1: Schematic setup of the nanofiber-based atom trap experiment. The red- and blue-detuned lasers are sent through the fiber to create the trap (see text). Light from outside the fiber (green arrow) scatters on the trapped cesium atoms (yellow cirles) and part of it is coupled to fiber-guided modes (green line). On one side, a single-photon detector is placed behind the cavity (see previous chapter). The magnetic offset field prevents spin-flips and allows to distinguish transitions between different Zeeman states [41]. Figure adapted from [13].

figure 3.1. A combination of attractive and repulsive potentials is used to create two diametric arrays of trapping sites. This is achieved by splitting the beam of a red-detuned laser and coupling it into the fiber from both sides. Both beams interfere to create a standing-wave potential. Additionally, a blue-detuned beam is sent through the fiber as a running wave, exerting a repulsive force on the atoms. Preparing the beams such that they are quasi-linearly polarized in the fiber with the polarization of the blue beam orthogonal to that of the red beams, results in individual trapping sites along both sides of the fiber [5, 14]. These trapping sites are about 500 nm apart and 230 nm from the surface of the fiber [42]. Typical parameters are a trap depth of 140 µK and calculated radial, azimuthal and axial trap frequencies of 120 kHz, 87 kHz and 186 kHz, respectively. A more comprehensive description of this setup is given in [5, 13, 14, 43].

To count the trapped atoms, they are irradiated with light from outside the fiber. Part of this light is scattered into fiber-guided modes [44], which is indicated with the green arrow and the green line in figure 3.1. The cavity is placed on one end of the fiber, before a single-photon counting module. This is described in more detail in section 3.3.

3.2 Light Scattering from Trapped Atoms

In this section, the scattering of light on trapped atoms is addressed with a focus on the heating of atoms through scattering. This is discussed in section 3.2.1. A

short introduction to cooling is given in section 3.2.2 as a means to counter-act this heating.

With the approximation of a two-level atom, the scattering rate Γ_s when irradiated with a near-resonant light field can be expressed as [26, 14]

$$\Gamma_s = \frac{\gamma}{2} \frac{\frac{I}{I_s}}{1 + \frac{I}{I_s} + \left(\frac{2\delta}{\gamma}\right)^2} \,, \tag{3.2}$$

where I is the intensity of the light field at the position of the atom, I_s is the free-space saturation intensity, γ is the natural decay rate of the excited state and δ is the detuning of the angular frequency of the laser. The saturation parameter $\frac{I}{I_s}$ is given by [45]

$$\frac{I}{I_s} = 2\frac{|\Omega|^2}{\gamma^2} \,, \tag{3.3}$$

where Ω is the Rabi frequency. For the calculations in this report, the $|F = 4\rangle \leftrightarrow |F' = 5\rangle$ transition of the cesium D2 line is used with $\gamma = 2\pi \cdot 5.2\,\mathrm{MHz}$ [26]. The reason why this transition is used is described in section 3.3.

3.2.1 Scattering-induced Heating

There are two different heating regimes that depend on the scattering rate. We define the case where the scattering rate is on the order of or below the trap frequencies as low-intensity regime. If the scattering rate is much higher than the trap frequencies, this is called high-intensity regime. In the following, the different heating effects for both regimes are derived.

In the low-intensity regime, the atom absorbs on average one or less photons per oscillation. This corresponds to an increase of its thermal energy by the recoil energy

$$E_{\mathrm{rec}} = \frac{1}{2}k_{\mathrm{B}}T_{\mathrm{rec}} \tag{3.4}$$

In equation 3.4, k_{B} is the Boltzmann constant and T_{rec} is defined as recoil temperature. Assuming the atom to be initially at rest, it's kinetic energy after the absorption is

$$\Delta E = \frac{(\hbar k)^2}{2m} \,, \tag{3.5}$$

where $\hbar k$ is the momentum of the absorbed photon and m is the mass of the atom. With $\Delta E = E_{\mathrm{rec}}$ and equations 3.4 and 3.5, we obtain

$$T_{\mathrm{rec}} = \frac{(\hbar k)^2}{k_{\mathrm{B}}m} \,. \tag{3.6}$$

After absorption, the atom will re-emit the photon in a random direction. This increases the kinetic energy of the atom again by E_{rec}, so that the overall increase in energy per scattering process is $2E_{\text{rec}}$[2] [36]. The thermal energy of the atom is given by

$$E = \frac{3}{2}k_{\text{B}}T \tag{3.7}$$

and the energy of the atom after time Δt can be expressed as

$$E(t + \Delta t) = E(t) + 2E_{\text{rec}}\Gamma\Delta t\,, \tag{3.8}$$

where $2E_{\text{rec}}$ is the energy difference per scattering event and $n = \Gamma\tau$ is the number of scattering events. Subtracting $E(t)$ and dividing by Δt leads with $\Delta t \to 0$ to

$$\dot{E} = 2E_{\text{rec}}\Gamma\,, \tag{3.9}$$

where $\dot{E}$ is the time derivative of E. With equations 3.7, 3.9 and 3.4, we obtain

$$\dot{T} = \frac{2}{3}T_{\text{rec}}\Gamma\,. \tag{3.10}$$

Inserting equation 3.6 and integrating over time finally yields

$$T(t) = \frac{2}{3}\frac{(\hbar k)^2}{k_{\text{B}}m}\Gamma t + T_0\,, \tag{3.11}$$

where T_0 is the initial temperature. Equation 3.11 describes heating in the low-intensity regime. Note that the temperature increase is linear in the number of scattered photons.

If, on the other hand, the scattering rate is significantly larger than the trap frequencies, the above result is not applicable any more. In this case, scattering occurs so fast, that the atom absorbs multiple photons during one oscillation in the trap. In fact, if the scattering rate is large enough, the atom is "pushed" out of the trap in a time much shorter than $\frac{1}{f_{\text{trap}}}$, where f_{trap} is the trap frequency. Each time the atom absorbs a photon, its momentum increases by the momentum $\hbar k$ of the photon. Since the absorptions happen so fast, the total momentum transfer to the atom can be written as $n\hbar k$ with n being the number of absorbed photons. Thus, equation 3.5 becomes

$$\Delta E = \frac{(n\hbar k)^2}{2m} = \frac{(\hbar k)^2}{2m}n^2\,. \tag{3.12}$$

---

[2]The incident photons all propagate in the same direction before absorption. Note that for simplicity, this anisotropy is neglected and equal distribution of kinetic energy over all three dimensions is assumed.

With equation 3.7, this yields

$$\Delta T = \frac{1}{3} \frac{(\hbar k)^2}{k_{\mathrm{B}} m} \Gamma^2 (\Delta t)^2 \,, \tag{3.13}$$

where we used $n = \Gamma \Delta t$. Equation 3.13 describes heating in the high-intensity regime.

Comparing equations 3.11 and 3.13, it can easily be seen that in the high-intensity regime, significantly less photons are needed to heat the atom out of the trap. In particular $n_{\mathrm{high}} = \sqrt{2 n_{\mathrm{low}}}$, which is consistent with [46]. Here, n_{high} and n_{low} are the number of photons needed in the high-intensity and low-intensity regime, respectively, to heat an atom by the same temperature.

To model the loss of atoms due to heating, the trap lifetime τ is used. We define the trap lifetime as the time, after which only $\frac{1}{e}$ of the initially trapped atoms remain and all others are lost. A simple estimate for τ is to use the average time needed to heat an atom out of the trap.

3.2.2 Cooling of Trapped Atoms

The heating effects described in section 3.2.1 lead to a loss of atoms from the trap. This can be countered by cooling the atoms.

In principle, the cooling of atoms in the nanofiber-based trap can be achieved by lasers from outside the fiber or, potentially, by lasers coupled into the fiber. A good overview of cooling methods and their quantitative treatment can be found in [45]. Here, only a very brief introduction to Doppler cooling is given.

For simplicity, we first consider the one-dimensional case with two counter-propagating laser beams that irradiate a single atom. Both lasers are red-detuned with respect to an atomic transition. There are three possibilities, the atom could be at rest or move towards either of the two lasers. If at rest, absorption of a photon is less likely than on resonance. If the atom moves towards one of the lasers, however, the probability of absorbing a photon emitted by this laser increases with its velocity due to the Doppler effect. Similarly, the probability of absorbing a photon emitted by the other laser, from which it is moving away, decreases. With each absorption, the atoms velocity is changed by the momentum of the photon. This leads to an effective slowing-down of the atom, no matter in which direction it moves. Note that there is a limit to this cooling process of $T_{\mathrm{D}} = \frac{\hbar \gamma}{2 k_{\mathrm{B}}}$, where T_{D} is the Doppler temperature [45]. In three dimensions, this could be achieved with three pairs of counter-propagating beams.

Referring to the trap lifetime τ introduced in section 3.2.1, the effect of cooling results in an increase of τ and for the purposes of this report, it is assumed that cooling leads to $\tau \gg t_{\mathrm{M}}$, where t_{M} is the duration of the measurement.

3.3 Atom Counting

This section covers the counting of atoms in the nanofiber-based trap. An overview of different experimental approaches to achieve this is given below.

The basic idea, shared by all experimental approaches outlined in the following, consists of irradiating the atoms with a probe beam and detection of the scattered photons. There are two different ways to irradiate the atoms, by sending the probe beam through the fiber or by using a beam that is focused on the atoms from outside the fiber. In both cases, the atoms scatter light into free-space as well as into fiber-guided modes [10, 44], yielding two possibilities of detection.

First, the case of the probe propagating in the fiber is discussed. If the light scattered into guided modes is measured, one invariably detects light from the probe beam itself as well. It is not possible to filter out the probe beam because it has the same frequency like the scattered light[3]. Even placing the detector so that it only detects light counter-propagating with respect to the probe, would still lead to detection of probe light due to reflections (e.g. at the fiber end facet).

Measuring light scattered out of the fiber, e.g. by means of a CCD camera as done in [47, 48], would not yield this problem. This would require a very sensitive low-noise CCD camera. Alternatively, it is possible to not measure the scattered light but the absorption of the probe when sent through the fiber. With increasing power of the probe, the cesium atoms saturate at scattering rates of $\frac{\gamma}{2}$, where γ is the spontaneous decay rate. At this point, the absorption does not change any more when the power is further increased. This saturation measurement then allows to infer the number of trapped atoms as done in [5].

Finally, the probe light could be directed at the atoms from outside the fiber to measure the light scattered into guided modes. The advantage of this approach is that, apart from the far-detuned trapping lasers, only the scattered light propagates in the fiber. A detector could then be placed on either end and the cavity of chapter 2 be used to filter out the background light due to Raman scattering. The atoms are then detected with a single-photon counting module. This setup is shown in figure 3.1 and is the basis for all following calculations.

The parameters that influence the accuracy of the measurement are the number of photons being detected, the number of dark counts of the detector and the heating of atoms, eventually leading to atom loss. All these mainly depend on the measurement time and scattering rate as variable parameters, while other parameters, like the detection efficiency are fixed by the setup. Therefore, the calculations presented in the next sections can easily be adapted for different experimental approaches by changing the parameters like e.g. the detection efficiency. Note that

---

[3]Note that this is not generally true as the probe could for example excite one transition and the measurement focus on the decay to another ground state. However, with the two-level approach taken in section 3.2.1, the scattered light has the same frequency as the probe.

only the total number of detected photons is important and that in principle detection on both ends of the fiber would be possible.

The filtering of the cavity has a significant effect on the resulting accuracy and this is discussed in section 3.3.7. Since there is only one cavity available, optimally all guided light should propagate towards the detector behind this cavity (cf. figure 3.1). This is possible by exploiting the spin-orbit coupling of light confined inside the nanofiber. The details of this process are not given here but can be found in [42, 49]. In the configuration shown in [42], $90\,\%$ of the light that is scattered into guided modes propagates in one direction, using the same setup as depicted in figure 3.1. This leads to a probability of $2.3\,\%$[4] that a scattered photon is coupled to a fiber-guided mode and propagates towards the detector behind the cavity. As shown in figure 3.1, atoms are trapped on both sides of the fiber and it should be noted that this effect leads to preferential scattering of light towards the detector for atoms on one side, while atoms on the other side scatter most photons away from the detector [42]. Thus, only atoms on one side of the fiber can be efficiently detected with this configuration.

In the following sections, three methods are presented to infer the number of trapped atoms. To analyse the differences and the accuracy of these methods, they are used on simulated data. The simulation of this data is described in section 3.3.1. Then, all three methods are introduced and their performances analysed in sections 3.3.2, 3.3.3 and 3.3.4. Most calculations in this chapter are based on scattering rates comparable to the trap frequencies, which corresponds to the low-intensity regime (cf section 3.2.1). The case of the high-intensity regime is discussed in section3.3.6. Finally, the effects of the cavity finesse and overall detection efficiency are discussed in sections 3.3.7 and 3.3.8.

3.3.1 Simulation of Experimental Results

A Monte Carlo simulation is run to generate data for the single-photon detector behind the cavity. The simulation starts with a given number N_A of trapped atoms and assumes that the mean number of detected signal photons in time interval Δt is

$$\langle R_\mathrm{S} \rangle \Delta t = P_\mathrm{det} P_\mathrm{sc} \Gamma N_\mathrm{A} \Delta t\,. \tag{3.14}$$

Here, $\langle R_\mathrm{S} \rangle$ is the mean rate of detected signal photons and P_det is the probability of detecting a photon that is propagating in the nanofiber towards the detector. P_sc is the probability that a scattered photon couples to a fiber-guided mode and propagates towards the detector. Thus $P_\mathrm{det}P_\mathrm{sc}$ gives the overall probability of detecting a scattered photon. Γ is the scattering rate and $\Gamma N_\mathrm{A} \Delta t$ gives the total

---

[4]This number follows from calculations based on the equations in [49] for the current setup of the nanofiber-based trap.

number of scattered photons in time Δt. Additionally to the signal photons, the detector also measures background photons (cf. section 2.1.1) and dark counts. Both are assumed to have constant rates that are determined from experiment and the sum of both is $\langle R_\mathrm{B} \rangle \Delta t$.

The probability to detect exactly k photons in a time interval Δt is given by a Poisson distribution

$$P_{\mathrm{S},\Delta t}(k) = \frac{e^{-\langle R_\mathrm{S} \rangle \Delta t}(\langle R_\mathrm{S} \rangle \, \Delta t)^k}{k!} \, . \tag{3.15}$$

The probability of counting at least one signal photon is then

$$P_{\mathrm{S},\Delta t}(k \geq 1) = 1 - P_{\mathrm{S},\Delta t}(0) = 1 - e^{-\langle R_\mathrm{S} \rangle \Delta t} \, . \tag{3.16}$$

The same applies for the background photons and dark counts.

Due to heating effects, atoms are lost during the measurement. This can be described by the trap lifetime τ with

$$N_\mathrm{A}(t) = N_{\mathrm{A},0} e^{-\frac{t}{\tau}} \, , \tag{3.17}$$

where $N_{\mathrm{A},0}$ is the number of initially trapped atoms. The average number of lost atoms within interval $[t, t + \Delta t]$ is then

$$\langle \Delta N_\mathrm{A}(t, \Delta t) \rangle = N_{\mathrm{A},0} \left(e^{-\frac{t}{\tau}} - e^{-\frac{t+\Delta t}{\tau}} \right) = N_\mathrm{A}(t) \left(1 - e^{-\frac{\Delta t}{\tau}} \right) \approx N_\mathrm{A}(t) \frac{\Delta t}{\tau} \, . \tag{3.18}$$

Analogously to equation 3.15, we then obtain the probability of loosing an atom as

$$P_{\mathrm{A},\Delta t}(k \geq 1) = 1 - e^{-N_{\mathrm{A},t} \frac{\Delta t}{\tau}} \, , \tag{3.19}$$

where $N_{\mathrm{A},t}$ is the actual number of remaining atoms at time t.

The simulation then proceeds by moving through time over an interval from $0 \, \mathrm{ms}$ to $200 \, \mathrm{ms}$ in steps of Δt and performs the following steps.

1. Create a random variable ξ between 0 and 1.

2. If $\xi < P_{\mathrm{S},\Delta t}(k \geq 1)$, a signal photon has been detected. Append (1) to the array of signal photons.

3. Else, no photon has been detected. Append (0) to the array of signal photons.

The same is done for background counts and lost atoms. In the case of lost atoms, the atom number N_A is decreased as well, which influences the rates for atom loss and signal counts (see above). Δt needs to be very small so that the probability of loosing one atom within this interval is much higher than loosing more than one atom. This is necessary to later compare the real number of trapped atoms with

the inferred number. However, if Δt is chosen too small, the simulation will need too long to run and the created data files will be unnecessarily large. Note that for the purpose of a rough estimation, detector saturation and dead time are not considered in this approach.

The result consists of three arrays that correspond to equal time steps of Δt and each element containing a 1 signifies a detector count or atom loss. All other elements are zeros. The sum of all array elements gives the total number of counts. An exemplary result of such a simulation is shown in figure 3.2.

(a) Detector Counts (b) Number of trapped atoms
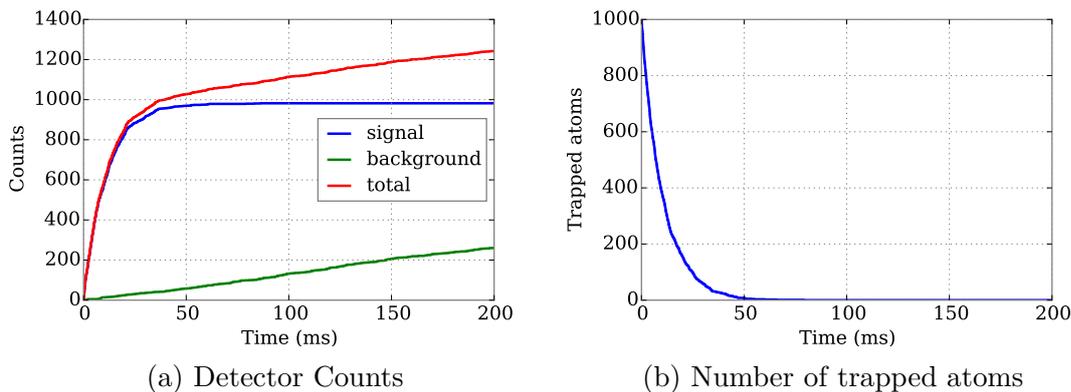
Figure 3.2: (a) Shown are the cumulative sums of the arrays for simulated signal counts and background counts. The background (green) shows a linear increase which is due to a constant rate of background counts (see text). The signal counts saturate when all atoms are lost.
(b) Shown is the number of atoms trapped along the fiber. As the simulation progresses, atoms get lost due to heating until finally no atoms are left.

The parameters used for this and all other simulations are given in table 3.1. Note that the number of detected signal photons is below the number of initially trapped atoms (cf. figure 3.2). This drastically limits the accuracy with which the number of atoms can be determined.

3.3.2 Fitting Approach

In the previous section, the generation of simulated data was described. A first method to analyse this data and infer the number of trapped atoms is given in this section. It consists of fitting a model to the total counts shown in figure 3.2a with the number of initially trapped atoms as the variable to optimize. The rate

Parameter	Value	Description
$N_{A,0}$	30 or 1000	Number of initially trapped atoms.
Γ	87 kHz	Scattering rate in low-intensity regime.
		This corresponds to the smallest trap frequency (cf. section 3.1).
P_{det}	5 %	Probability of detecting a photon that is
		in the nanofiber and propagating towards the detector.
P_{sc}	2.3 %	Probability that a scattered photon couples to a
		guided mode and propagates towards the detector.
T_0	30 µK	Mean temperature of atoms in trap.
T_{trap}	140 µK	Depth of trap.
Δt	2 µs	Time step of simulation.
$\langle R_B \rangle$	1.5 kHz	Sum of photons from fiber background and detector dark counts.

Table 3.1: Parameters as they were used in the simulation.

of total detector counts after measuring for time t is

$$\dot{N}_{tot}(t) = \underbrace{N_A(t)\Gamma P_{det} P_{sc}}_{\langle R_S \rangle} + \langle R_B \rangle \, , \tag{3.20}$$

where $N_A(t)$ is given by equation 3.17 and the other parameters were introduced in section 3.3.1. The number of total detector counts is then obtained by integrating over the measurement time t

$$N_{tot}(t) = \Gamma P_{det} P_{sc} \int_0^t N_A(t') \mathrm{d}t' + \langle R_B \rangle t \, . \tag{3.21}$$

With

$$\int_0^t N_{A,0} e^{-\frac{t'}{\tau}} \mathrm{d}t' = N_{A,0}\tau \left(1 - e^{-\frac{t'}{\tau}} \right) \, , \tag{3.22}$$

this becomes

$$N_{tot}(t) = \Gamma P_{det} P_{sc} N_{A,0}\tau \left(1 - e^{-\frac{t}{\tau}} \right) + \langle R_B \rangle t \, . \tag{3.23}$$

Except for the initial number of trapped atoms, $N_{A,0}$, all other parameters are calculated based on the assumptions discussed above and the average background count rate $\langle R_B \rangle$ is taken from a measurement. Fitting this model to the data shown in figure 3.2a results in an estimate of the initially trapped atom number of 1088[5], which is above the actual number of 1000 used in the simulation. This fit is shown in figure 3.3.

To better judge the performance of this method, the simulation is run multiple times. The results of fitting to these datasets are shown in figure 3.4. It can

---

[5]The uncertainty of the fit as returned by python's fit routine is below one atom. Bootstrapping leads to the same result. However, one should be careful with the significance of this result. A better estimate for the accuracy of the result is a standard deviation of 42 (cf. figure 3.4).
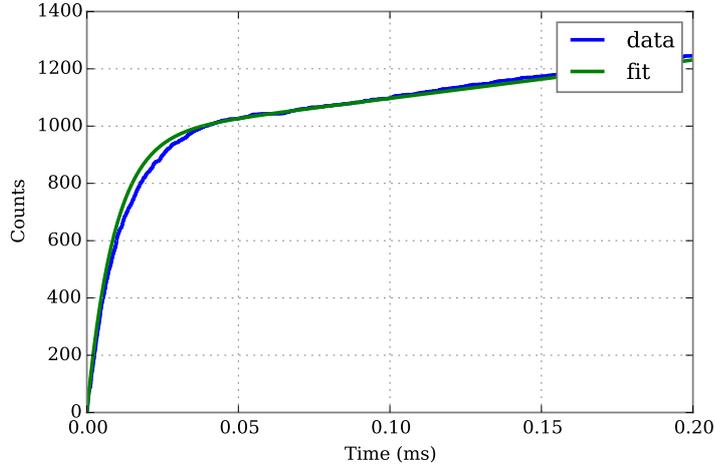
Figure 3.3: Fitting equation 3.23 to the total detector counts with free parameter $N_{A,0}$. The actual number of initially trapped atoms for this simulation was 1000 and the fit yielded 1088.

be seen that the number of trapped atoms tends to be underestimated with this method.

Note that since the above fit is using all simulated data, even at time-scales where all atoms are lost, this corresponds to a destructive measurement in the sense that no atoms would be left for further experiments. The performance of this method with increasing measurement time is shown in section 3.3.5.

As mentioned in section 3.2.2, the cooling of atoms during the measurement can be modelled with a large trap lifetime τ. In equation 3.23, the exponential term can be approximated as $e^{-\frac{t}{\tau}} \approx 1 + \frac{t}{\tau}$, which leads to

$$N_{\text{tot,cool}}(t) = \Gamma P_{\text{det}} P_{\text{sc}} N_{A,0} t + \langle R_B \rangle t \, . \tag{3.24}$$

The result of fitting to data simulated in this way is shown in figure 3.5. The standard deviation has now reduced from 12 atoms to 1.5 atoms and would improve even more for longer measurement times.

3.3.3 Optimal Probing Time

At the start of a measurement, the signal from the atoms is strongest with respect to the background counts. As atoms are lost, the signal becomes weaker and the influence of the background relatively stronger. When all atoms are lost, only the background leads to additional counts and the measurement accuracy can not be improved any more but will be worsened by taking more data. It thus makes

(a) 1000 atoms, 10000 datasets   (b) 30 atoms, 100 datasets
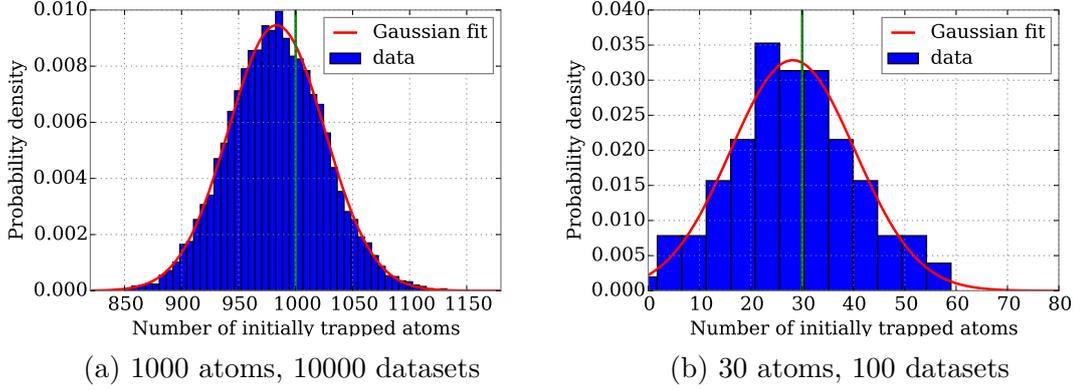
Figure 3.4: Fitting equation 3.23 to different datasets with 30 and 1000 initially trapped atoms. The histogram data is normalized and shows a Gaussian distribution. The vertical lines indicate the true number of initially trapped atoms.
(a) The mean value is 983 atoms with a standard deviation of 42 atoms.
(b) The mean value is 28 atoms with a standard deviaton of 12 atoms.

sense to assume that there is an optimal duration of measurement, for which the accuracy is best. An estimation for this optimal pulse time is derived in this section.

Starting with equation 3.23, we can solve for the initial number of trapped atoms

$$N_{\mathrm{A},0} = \frac{N_{\mathrm{tot}} - \langle R_{\mathrm{B}} \rangle t}{\Gamma P_{\mathrm{det}} P_{\mathrm{sc}} \tau \left(1 - e^{-\frac{t}{\tau}}\right)} \; . \tag{3.25}$$

In equation 3.25, N_{tot} is measured, while all other quantities are calculated or estimated. The uncertainty of this result depends on the uncertainty of the parameters, in particular on the uncertainty of the mean rate of background counts $\langle R_{\mathrm{B}} \rangle$ and the uncertainty of the measured data itself. For simplicity, we assume that the other parameters, like the trap lifetime τ only negligibly influence the uncertainty of the initial atom number. The variance of $N_{\mathrm{A},0}$ can then be calculated as

$$\sigma_{N_{\mathrm{A},0}}^2 = \left(\frac{1}{\Gamma P_{\mathrm{det}} P_{\mathrm{sc}} \tau \left(1 - e^{-\frac{t}{\tau}}\right)}\right)^2 \sigma_{N_{\mathrm{tot}}}^2 + \left(\frac{t}{\Gamma P_{\mathrm{det}} P_{\mathrm{sc}} \tau \left(1 - e^{-\frac{1}{\tau}}\right)}\right)^2 \sigma_{\mathrm{B}}^2 \; , \tag{3.26}$$

where σ_{B}^2 is the variance of the background counts $\langle R_{\mathrm{B}} \rangle t$. Since both, the background counts and the measured count rate, are described by a Poisson distribu-
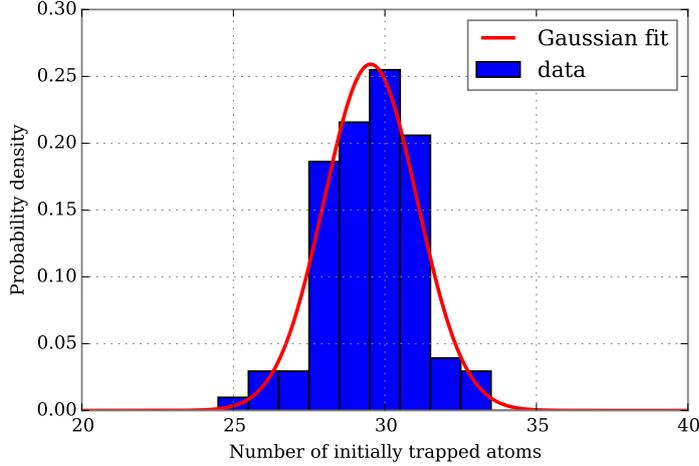
Figure 3.5: Fitting to the datasets of simulations with 30 atoms, whilst cooling them so that no atoms are lost. The measurement time is 200 ms and the mean value is 29.5 atoms with a standard deviation of 1.5 atoms.

tion, their variance is equal to their mean

$$\sigma^2_{N_{\text{tot}}} \approx \Gamma P_{\text{det}} P_{\text{sc}} N_{\text{A},0} \tau \left(1 - e^{-\frac{t}{\tau}}\right) + \langle R_{\text{B}}\rangle t \,, \tag{3.27}$$

$$\sigma^2_{\langle R_{\text{B}}\rangle} = \langle R_{\text{B}}\rangle t \,, \tag{3.28}$$

where we used the approximation that the measured value of the detector counts is roughly equal to the expected value. Equation 3.26 can then be written as

$$\sigma^2_{N_{\text{A},0}} = \frac{N_{\text{A},0}}{\Gamma P_{\text{det}} P_{\text{sc}} \tau \left(1 - e^{-\frac{t}{\tau}}\right)} + 2 \frac{\langle R_{\text{B}}\rangle t}{\left[\Gamma P_{\text{det}} P_{\text{sc}} \tau \left(1 - e^{-\frac{t}{\tau}}\right)\right]^2} \,. \tag{3.29}$$

Plotting the so-calculated variance for a range of measurement times indeed shows an optimal time. This is shown in figure 3.6. It is not analytically possible to determine the optimal time t_{opt}, for which the variance in equation 3.29 is minimized. Therefore, this is in the following always numerically calculated.

For the special case of cooling, the trap lifetime is much larger than the measurement time and thus we can simplify the variance to

$$\sigma^2_{N_{\text{A},0,\text{cool}}} = \frac{N_{\text{A},0}}{\Gamma P_{\text{det}} P_{\text{sc}} t} + 2 \frac{\langle R_{\text{B}}\rangle}{\left[\Gamma P_{\text{det}} P_{\text{sc}}\right]^2 t} \,, \tag{3.30}$$

by using the Taylor expansion for the exponential. It is now clear that the variance improves with increasing measurement time. However, this is only true for $t \ll \tau$.
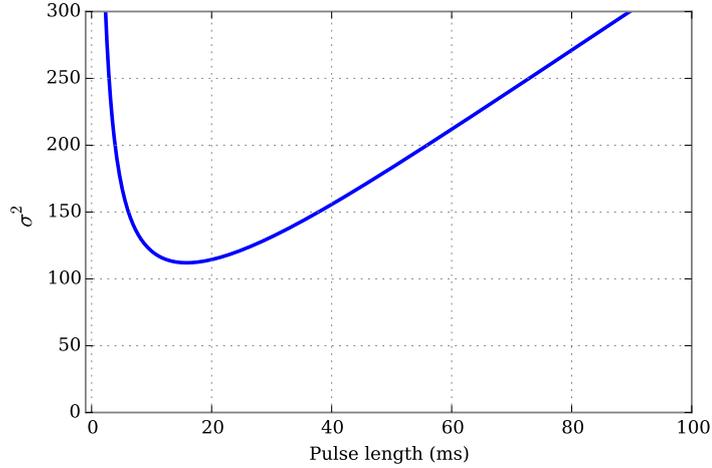
Figure 3.6: Variance of the number of initially trapped atoms in dependence of measurement time. The minimal variance of 112 is at $t = 16\,\text{ms}$. This calculation is for 30 atoms.

The result of determining the number of initially trapped atoms as described in this section is shown in figure 3.7. The mean value and standard deviation agree very well with the fitting approach (cf. section 3.3.2), indicating that both methods are equal in precision. The standard deviation of the data in figure 3.7b is 9 and the calculation with equation 3.29 gives 10, which is in very good agreement. For the data in figure 3.7a, it is 41 while the calculation gives 35. This method, like the fitting approach, also tends to underestimate the atom number.

3.3.4 Bayesian Inference

The approach described in this section is based on Bayes' law. This is in the following briefly derived. Let the probability of event A be $P(A)$ and the conditional probability of event B when A is already true $P(B|A)$. Then, the probability of A and B being true simultaneously is

$$P(A, B) = P(A|B)P(B) = P(B|A)P(A).$$ (3.31)

From this, we get

$$P(A|B) = \frac{P(B|A)P(A)}{P(B)},$$ (3.32)

which is called Bayes' law. Before discussing the implications of this further, we will substitute A and B with parameters relevant for the counting of atoms. For

(a) 1000 atoms, 10000 datasets

(b) 30 atoms, 100 datasets
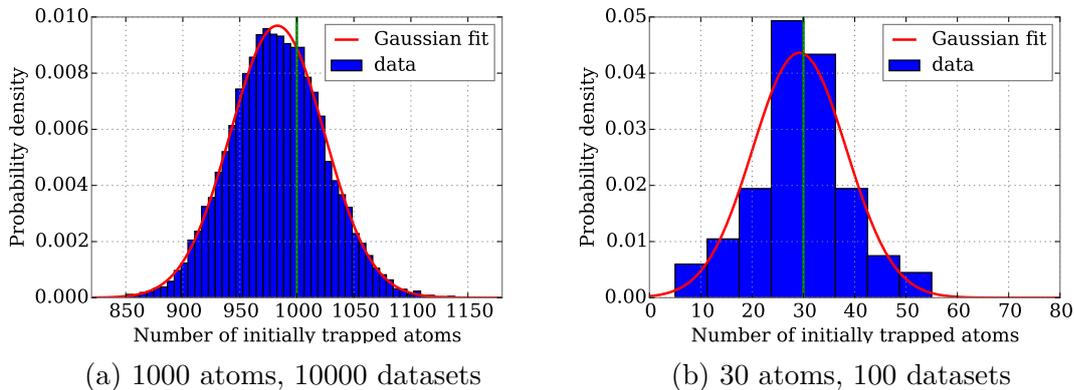
Figure 3.7: Determination of the number of trapped atoms with equation 3.25. The histogram data is normalized and shows a Gaussian distribution. The vertical lines indicate the true number of initially trapped atoms. (a) The mean value is 983 atoms with a standard deviation of 41 atoms. (b) The mean value is 29 atoms with a standard deviaton of 9 atoms.

A, we set the number of initially trapped atoms $N_{A,0}$ and for B the number of detector counts N_{tot}. Bayes' law then becomes

$$P(N_{A,0}|N_{tot}) = \frac{P(N_{tot}|N_{A,0})P(N_{A,0})}{P(N_{tot})} \, . \tag{3.33}$$

The term $P(N_{A,0}|N_{tot})$ gives the probability of having $N_{A,0}$ initially trapped atoms when N_{tot} detector counts were measured. This is called posterior probability and is exactly what we are interested in. $P(N_{tot}|N_{A,0})$ is the so-called likelihood and represents the probability to measure N_{tot} detector counts when $N_{A,0}$ atoms are trapped on the nanofiber. This is multiplied with the prior $P(N_{A,0})$, the probability of $N_{A,0}$ atoms being trapped. Finally, the probability is normalized by dividing with the probability of N_{tot} detector counts $P(N_{tot})$. A more comprehensive introduction to Bayesian statistics can be found in [50] and practical cases in [51, 52].

The posterior probability estimate can be improved by Bayesian inference. After obtaining a posterior probability distribution, it can be used as new prior with new measurement data to get an improved posterior distribution. In this way, the posterior will get more and more accurate with each iteration. The calculation consists of the following steps.

1. Guess initial prior. For simplicity, a flat initial distribution is assumed. Using a Gaussian distribution centered at the atom number determined with the fitting approach of section 3.3.2 and a variance calculated with equation 3.29, does not lead to better end results.

2. Compute the likelihood based on equation 3.25.

3. Repeat steps 1 and 2 for many values of $N_{A,0}$

4. Multiply both results and normalize the distribution

5. Use the so-obtained posterior as new prior and start again with new data to compute an improved posterior distribution.

To do this, the measured data is divided into slices. As an example, the data shown in figure 3.3 is divided into slices of equal time so that all counts detected in the first 10 µs belong to the first slice, all counts detected between 10 µs to 20 µs to the second slice and so forth. Then, the Bayesian inference method is used to compute a posterior from the first slice. This is used as prior to determine the posterior of the second slice and so on. Alternatively, one could divide the slices by equal count rates, e.g. every slice contains 100 counts but the time ranges of the slices vary significantly. In the first case the likelihood would answer the question "how likely is it that there were N counts in this interval"?. In the second case the question would be "how likely is it that the next N counts were detected within the time-interval $[t_1, t_2]$?". Of these, the latter, with slices of equal count rates, has been found to perform better.

The results of such an analysis are shown in figure 3.8 and are very similar to the ones obtained in the previous sections. Again, the actual value of initially trapped atoms is underestimated. This is discussed further in section 3.3.5.

One parameter of the Bayesian inference is the "step length", corresponding to the number of detector counts per slice. Figure 3.9 shows the results of varying this step length from 1 to 950 for simulations with 1000 atoms. For small step lenghts, the performance drops significantly. This can be explained by there being too few counts per slice to reasonably use statistical methods. For very large step lengths, the performance increases. In these cases, since the step length is so big, there is only one big slice and Bayes' law is only applied once. Indeed, a slight improvement of the analysis algorithm can be seen for this case but it is not significant. When analysing a large set of simulations of 1000 trapped atoms, the deviations of the mean value for different step lengths are on the order of one atom, compared to a standard deviation of about 40 atoms.

3.3.5 Comparison of Analysis Methods

In the previous sections, three methods to determine the number of trapped atoms were introduced. All are based on the same model (cf. equation 3.23) and yield similar results. Figure 3.10 shows a real-time analysis using simulated data of 1000 trapped atoms with all three methods. Real-time means that the data is analysed

(a) 1000 atoms, 10000 datasets   (b) 30 atoms, 100 datasets
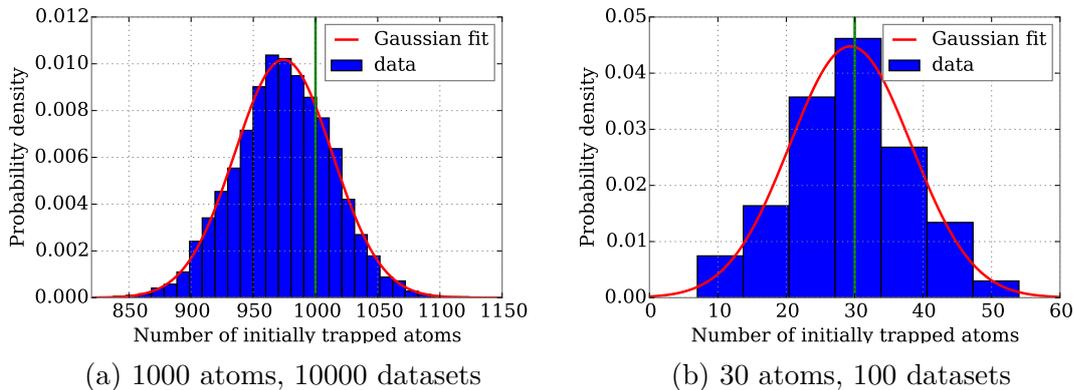
Figure 3.8: Number of initially trapped atoms as computed with Bayesian inference. The histogram data is normalized and shows a Gaussian distribution. The vertical lines indicate the true number of initially trapped atoms. (a) The mean value is 974 atoms with a standard deviation of 39 atoms.
(b) The mean value is 29 atoms with a standard deviaton of 9 atoms.

as if it was measured during the simulation and the accuracy of the determined atom number is improved as the measurement proceeds. It can be seen that all three methods show very similar behaviour in the estimation of the current atom number (cf. figure 3.10a) but the final guess of the number of initially trapped atoms varies significantly (cf. figure 3.10b). It can also be seen that the likelihood (cf. section 3.3.4) has a strong effect on the Bayesian estimate during the first half of iterations, while it induces almost no changes from iteration 30 onward (cf. figure 3.10b). This can be explained by the fact that most atoms are lost at that point and the data in the last analysed intervals is only weakly dependent on the initial number of trapped atoms. This means that for example, starting with 1000 atoms or starting with 1200 atoms would only lead to insignificant changes in these intervals. The likelihood distribution is then extremely flat and does not change the prior by much.

So far, these methods were only employed on reasonable datasets. Figure 3.11 shows the result of using them on a dataset with no signal counts—but with background counts. All three, when interpreting negative values as 0, perform well on this data. The fitting approach performs best, correctly interpreting each dataset when setting negative results to 0.

Finally, an analysis of data with very high background counts is shown in figure 3.12. In these extreme cases, all methods significantly underestimate the atom number. The fitting approach, however, performs worst, giving results that are several hundred atoms below the results of the other methods.
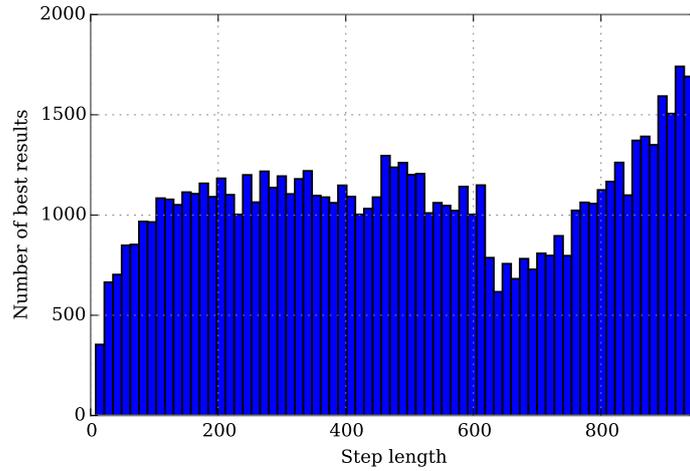
Figure 3.9: Number of best results in dependence of the Step length for Bayesian inference. This is computed by analysing each simulation result multiple times with different step lengths. All those that lead to the closest atom number with respect to the real one are marked as "best result". Thus, one simulation can have more than one best result. All step lengths are shown on the x-axis, while the y-axis shows the number of occurrences of best result. All simulations used an atom number of 1000.

To conclude, three methods to infer the number of trapped atoms were presented in the previous sections. They are all based on the same model and lead to similar results when applied to many datasets. However, for a specific dataset, they lead in general to significantly different atom numbers. The underestimation common to all these methods can be explained by the background rate. When it is increased, the effect of underestimation is stronger. At very high background rates, the fitting approach performs significantly worse compared with the other two methods.
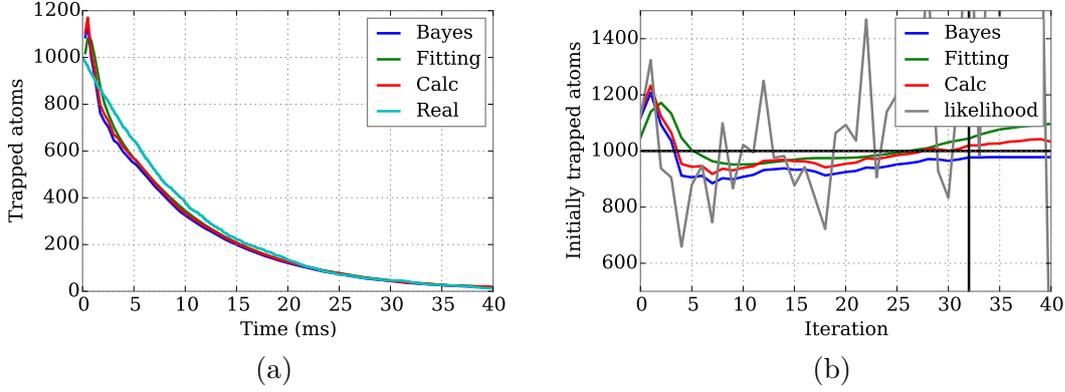
Figure 3.10: (a) Real-time estimation of the current number of trapped atoms along the nanofiber using a simulated measurement.

(b) Real-time estimation of the number of initially trapped atoms using the same dataset as for (a). Shown are the estimations based on Bayesian inference, the fitting approach and the calculation with equation 3.25. The likelihood curve corresponds to the atom numbers of maximal likelihood in Bayesian inference. The x-axis shows the iteration number in Bayesian inference.

The straight line in (b) at 1000 atoms and the curve labeled "Real" in (a) give the actual number of trapped atoms. The vertical line in (b) marks the optimal measurement time t_{opt} (cf. section 3.3.3).
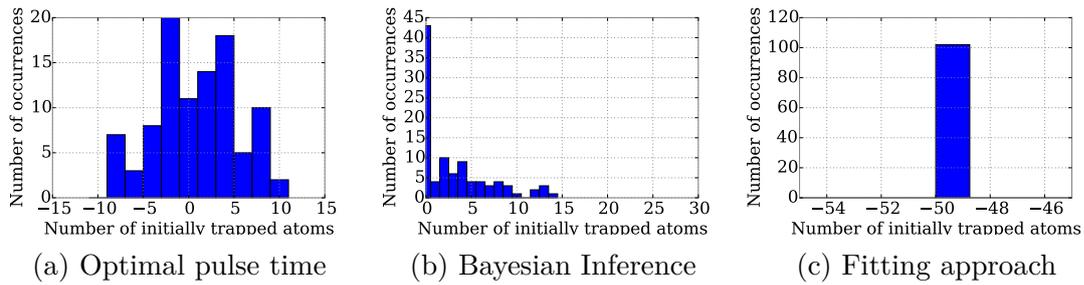
Figure 3.11: Results of using all three methods on datasets that contain only background counts but no signal counts.
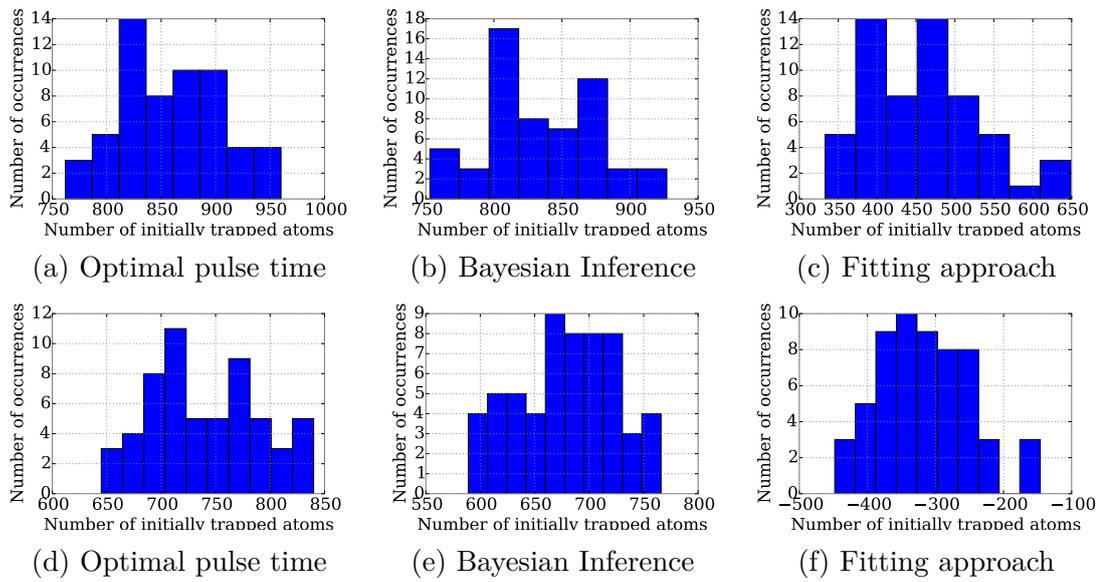
Figure 3.12: Results of using all three methods on datasets with 1000 atoms that contain very high background counts.
(a) - (c) The background count rate is roughly 60 % of the signal count rate at the beginning.
(d) - (f) The background count rate is larger than the signal count rate.

68

3.3.6 Dependence on Scattering Rate

In section 3.2.1, the two different heating regimes for low and high scattering rates were introduced. Using equation 3.29, the variance of the measurement can be estimated for both regimes. This is shown in figure 3.13. For the low-intensity

(a) Low intensity
(b) High intensity
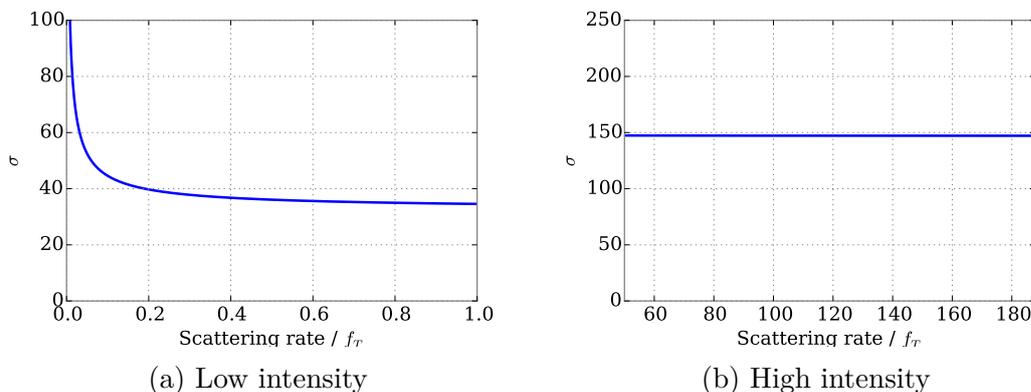
Figure 3.13: Square-root of variance as calculated with equation 3.29 in dependence of the scattering rate for 1000 atoms. f_T is the lowest trap frequency ($87\,\mathrm{kHz}$). The calculations are done using the optimal pulse time for each scattering rate as described in section 3.3.3. The maximal scattering rate of $\frac{188}{f_T}$ in (b) corresponds to $\frac{\gamma}{2}$, where γ is the natural linewidth.

regime, the accuracy improves with increasing scattering rate. The reason for this improvement is the decreasing optimal measurement time with increasing scattering rate. This means that there are less background counts detected while the amount of signal counts stays roughly the same. Thus, the signal-to-noise ratio increases with the scattering rate, leading to more accurate results. In the high-intensity regime, the standard variation is roughly constant and independent of the scattering rate. As for the low-intensity regime, the optimal measuring time decreases with increasing scattering rate but since the atoms are lost much faster, there is only a fraction of the signal counts detected. The background counts have almost no influence on the total number of counts, since the measurement times are very short. Therefore, the low-intensity regime leads to better accuracy.

3.3.7 Effect of Cavity

In equation 3.29, an estimation of the variance was given. This depends on the amount of background counts detected during the measurement. Figure 3.14 depicts the standard deviation for a reduction by a factor of 2. This could be achieved

69

with a higher finesse of the cavity by using mirrors with higher reflectivity. It can be seen that this reduction leads to better accuracy. Note that further reduction does not change the accuracy significantly. The reason for this is that the second term in equation 3.29 is already much smaller than the first for a reduction by half and does not influence the variance by much any more. Furthermore, the cavity does not only reduce the background counts, it also attenuates the power of the signal[6]. This has two opposing effects. The suppression of the background counts leads to an improvement of the accuracy while the lower detection efficiency of signal photons leads to worse accuracy (cf. section 3.3.8). Additionally, the variance is proportional to the number of trapped atoms, while the background counts are not influenced by this. Therefore, the higher the number of trapped atoms is, the smaller is the effect of background counts on the variance. As shown in figure 3.14, this results in an improvement with cavity for atom numbers below about 1000 but for atom numbers above 1000, the results without cavity are better.
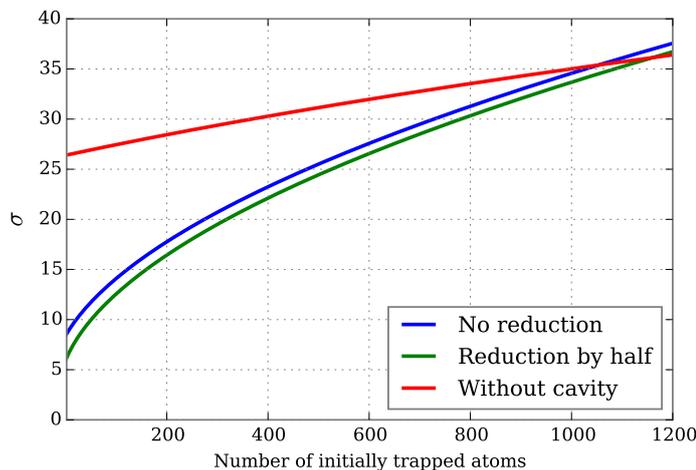
Figure 3.14: Standard deviation (cf. equation 3.29) in dependence of atom number. The graphs show the effects of a reduction of background counts by a factor of 2 and the effect of the cavity.

3.3.8 Effect of Detection Efficiency

The detection efficiency for photons inside the nanofiber that propagate towards the detector is about 5 %. The effect of changing detection efficiency on the estimated standard deviation for the counting of atoms is shown in figure 3.15. An

---

[6]As described in section 2.5, the overall transmission through the cavity setup is 44 %.

increase of the detection efficiency results in more signal photons being detected and thus improves the signal-to-noise ratio and leads to more accurate measurements. Currently, there is a 50:50 beamsplitter in front of the cavity (cf. section 3.1). Removing it, would almost halve the standard deviation for 30 trapped atoms.
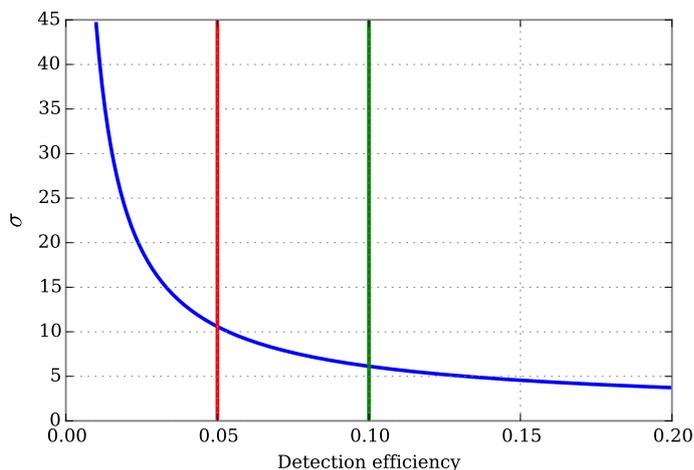
Figure 3.15: Influence of detection efficiency on variance estimation. The variance is calculated with equation 3.29 for 30 trapped atoms. The vertical lines correspond to the current detection efficiency (red) and the achievable detection efficiency (green) when bypassing the 50:50 beamsplitter in front of the cavity (see figure 3.1). Detection efficiency means the probability of detecting a photon that is in the nanofiber and propagates towards the detector.

3.4 Conclusion

This chapter focussed on possible ways to count atoms trapped along a nanofiber. Three methods were investigated and their performance evaluated with a Monte Carlo simulation. All three yield similar results but the fitting approach described in section 3.3.2 performs significantly worse than the other two for high rates of background counts. Bayesian inference and the approach using an optimal probing time are therefore more robust to such changes. With these methods, it would be possible to determine the atom number with a standard deviation of 9 for about 30 trapped atoms when using the cavity of chapter 2.

Good results are obtained when measuring long enough so that most atoms

are lost due to heating. Better accuracy and almost no atom loss during the measurement could be achieved by cooling the atoms while measuring them or even use the cooling lasers as probe beam to determine the atom number. In such a measurement, the variance decreases with time[7] as $\sigma^2 \propto t^{-1}$. With this approach, even single-atom accuracy would be possible.

The main factors that influence the accuracy are the transmission through the cavity and and the suppression of background counts. While a further suppression of background does only yield limited improvement, an increase in the signal transmission could lead to much better accuracy. As an example, a reduction in variance of almost a factor of 4 for low atom numbers could be achieved by removing a 50:50 beam splitter, which is currently placed in the beam path and used for other experiments.

The experimental schemes introduced in this chapter focussed on the scattering of a probe beam on the atoms and detecting the scattered photons. Another possible approach is taken in [52], where the accumulated phase-shift through interaction with the atoms in the evanescent field is used to infer the number of trapped atoms around a nanofiber. With this method, they achieve accuracies of ± 8 for about 1000 trapped atoms based on Bayesian inference similar to how it is used in section 3.3.4. Besides their different experimental approach, they start with almost 3000 atoms and measure until about 2000 of these are lost to determine the number of atoms that are still left. The methods discussed in this chapter, however, focus on the inference of the number of initially trapped atoms. It is likely that such an approach of not infering the initial number but the number after the measurement would also result in much higher accuracies for the experimental setup discussed in this report. This has not yet been investigated.

---

[7]This is only true in the approximation $t \ll \tau$, where t is the measurement time and τ the trap lifetime.

4 Summary

In the course of this Master's thesis, an FPI was set up that is actively stabilized to a reference laser. The purpose of this cavity is to filter out background light from the fiber, which is caused by Raman scattering and fluorescence. Additionally, it strongly suppresses the control field in EIT experiments. Measurements show that it reduces the fiber background by $(98.5 \pm 0.7)\,\%$ and strongly attenuates the control beam, resulting in a measured power of $-42.7\,\mathrm{dB}$ with respect to the power of the fundamental mode. The suppression of the fiber background is found to be independent of the FSR for the region of interest. Transmission through the whole cavity setup, including the fiber-coupling on both ends, yields $44\,\%$ transmission of the probe field. With fluctuations of less than $\pm 1\,\%$, the transmission through the cavity is very stable, even during long-term measurements of multiple hours.

In chapter 3, the use of this cavity filter to count atoms in a nanofiber-based trap has been investigated. While different experimental schemes are possible, the results in this report are based on directing a probe laser towards the atoms from outside the fiber and measuring the photons that are scattered into guided modes. Three methods to infer the number of trapped atoms are discussed and their results verified with data from a Monte-Carlo simulation. All these methods underestimate the number of atoms, which is mainly due to the signal-to-noise ratio. An increase of the background count rate, while keeping the detection rate of scattered photons fixed, leads to further underestimation of the atom number. Furthermore, these methods are destructive, meaning that during one measurement process almost all atoms are lost due to heating. This can be countered by cooling the atoms, which leads to a dependence of the variance on the measurement time as $\sigma^2 \propto t^{-1}$.

In general, the accuracy of the measured atom number improves strongly with the detection efficiency. This is discussed in section 3.3.8. As an example, doubling the current detection efficiency would reduce the variance almost by a factor of 4. Therefore, the use of the cavity leads to much better results for atom numbers below about 1000 because the cavity strongly suppresses the fiber background. For more than 1000 trapped atoms, the cavity does not improve the accuracy and even worsens it for larger atom numbers (cf. figure 3.14). This is due to the lower detection efficiency with the cavity in place[1]. Additionally, the variance is

---

[1] The overall transmission through the cavity is $44\,\%$.

proportional to the number of trapped atoms while the background counts are not. Thus, the relative influence of the background counts on the variance decreases with increasing atom number. Best results would be achieved when cooling the atoms during the measurement and possibly increasing the detection efficiency.

Bibliography

[1] Michael J. Renn et al. "Laser-guided atoms in hollow-core optical fibers". In: *Physical review letters* 75.18 (1995), p. 3253. DOI: 10.1103/PhysRevLett.75.3253.

[2] K. P. Nayak et al. "Cavity formation on an optical nanofiber using focused ion beam milling technique". In: *Optics express* 19.15 (2011), pp. 14040–14050. DOI: 10.1364/OE.19.014040.

[3] K. O. Hill et al. "Bragg gratings fabricated in monomode photosensitive optical fiber by UV exposure through a phase mask". In: *Applied Physics Letters* 62.10 (1993), p. 1035. DOI: 10.1063/1.108786.

[4] V. R. Supradeepa et al. "A high efficiency architecture for cascaded Raman fiber lasers". In: *Optics express* 21.6 (2013), pp. 7148–7155. DOI: 10.1364/OE.21.007148.

[5] E. Vetsch et al. "Optical Interface Created by Laser-Cooled Atoms Trapped in the Evanescent Field Surrounding an Optical Nanofiber". In: *Physical Review Letters* 104.20 (2010), p. 203603. DOI: 10.1103/PhysRevLett.104.203603.

[6] Danny O'Shea et al. "Fiber-Optical Switch Controlled by a Single Atom". In: *Physical Review Letters* 111.19 (2013). DOI: 10.1103/PhysRevLett.111.193601.

[7] A. Stiebeiner et al. "Ultra-sensitive surface absorption spectroscopy using sub-wavelength diameter optical fibers". In: *Optics Express* 17.24 (2009), pp. 21704–21711. DOI: 10.1364/OE.15.011952.

[8] J. Petersen, J. Volz, and A. Rauschenbeutel. "Chiral nanophotonic waveguide interface based on spin-orbit interaction of light". In: *Science* 346.6205 (2014), pp. 67–71. DOI: 10.1126/science.1257671.

[9] A. Ghatak and K. Thyagarajan. *An Introduction to Fiber Optics*. Cambridge University Press, 1998. ISBN: 9780521577854.

[10] Fam Le Kien, V. Balykin, and K. Hakuta. "Scattering of an evanescent light field by a single cesium atom near a nanofiber". In: *Physical Review A* 73.1 (2006). DOI: 10.1103/PhysRevA.73.013819.

[11] Florian Warken. "Ultradünne Glasfasern als Werkzeug zur Kopplung von Licht und Materie." PhD thesis. Bonn: Rheinische Friedrich-Wilhelms-Universität Bonn, 2007.

[12] G. Brambilla. "Optical fibre nanowires and microwires: a review". In: *Journal of Optics* 12.4 (2010), p. 043001. DOI: 10.1088/2040-8978/12/4/043001.

[13] R. Mitsch. "Interaction and manipulation of nanofiber-trapped atoms with spin–orbit coupled light". PhD thesis. Vienna Technical University, 2014.

[14] Guillem Sagué. "Cold atom physics using ultra-thin optical fibres". PhD thesis. Bonn: Friedrich-Wilhelms-Universität Bonn, 2008.

[15] David Wardle. "Raman scattering in optical fibres". Thesis. University of Auckland, 1999.

[16] Michael Fleischhauer, Atac Imamoglu, and Jonathan P. Marangos. "Electromagnetically induced transparency: Optics in coherent media". In: *Reviews of Modern Physics* 77.2 (2005), p. 633. DOI: 10.1103/RevModPhys.77.633.

[17] M. Vaughan. *The Fabry-Perot Interferometer: History, Theory, Practice and Applications.* Series in Optics and Optoelectronics. Taylor & Francis, 1989. ISBN: 9780852741382.

[18] Derek A. Long. *The Raman effect : a unified treatment of the theory of Raman scattering by molecules.* Chichester ua: Wiley, 2002. 597 pp. ISBN: 0471490288.

[19] Joseph R. Lakowicz. *Principles of Fluorescence Spectroscopy.* Springer, Dec. 5, 2007. 961 pp. ISBN: 9780387463124.

[20] Peter J. Larkin. *Infrared and Raman spectroscopy : principles and spectral interpretation.* Amsterdam ua: Elsevier, 2011. 228 pp. ISBN: 9780123869845.

[21] Wolfgang Demtröder. *Laser spectroscopy.* 4. Vol. 2. 2 vols. Springer, 2008. ISBN: 978-3-540-74952-3.

[22] Thomas Schneider. *Nonlinear optics in telecommunications : with 14 tables, and 70 problems.* Berlin ua: Springer, 2004. 415 pp. ISBN: 3540201955.

[23] E. Dianov. "New Raman Fibers". In: *Raman Amplifiers for Telecommunications 1.* Springer Series in Optical Sciences 90/1. Springer New York, 2004. ISBN: 978-0-387-00751-9.

[24] A. Kocharovskaya and Ya I. Khanin. "Population trapping and coherent bleaching of a three-level medium by a periodic train of ultrashort pulses". In: *Zh. Eksp. Teor. Fiz* 90 (1986), pp. 1610–1618.

[25] K.-J. Boller, A. Imamolu, and S. E. Harris. "Observation of electromagnetically induced transparency". In: *Phys. Rev. Lett.* 66.20 (May 1991), pp. 2593–2596. DOI: 10.1103/PhysRevLett.66.2593.

[26] Daniel A. Steck. "Cesium D line data". In: *Los Alamos National Laboratory (unpublished)* 124 (2003).

[27] H. Kogelnik and Tingye Li. "Laser beams and resonators". In: *Applied Optics* 5.10 (1966), pp. 1550–1567.

[28] B. Saleh and M. Teich. *Fundamentals of Photonics*. 2. Wiley, 2007. ISBN: 978-0-471-35832-9.

[29] Dieter Meschede. *Optik, Licht und Laser*. Wiesbaden: Vieweg + Teubner in GWV Fachverlage, 2008. ISBN: 9783835101432 3835101439 9783834892881 3834892882.

[30] Léon Georges Gouy. *Sur une propriété nouvelle des ondes lumineuses*. Gauthier-Villars, 1890.

[31] S. Feng and H. Winful. "Physical origin of the Gouy phase shift". In: *Optics letters* 26.8 (2001), pp. 485–487.

[32] Peter Herskind. "Cavity Quantum Electrodynamics with Ion Coulomb Crystals". PhD thesis. The University of Aarhus, Sept. 2008. 222 pp.

[33] L. Ricci et al. "A compact grating-stabilized diode laser system for atomic physics". In: *Optics Communications* 117.5 (1995), pp. 541–549.

[34] Daniel A. Steck. "Rubidium 87 D line data". In: (2001).

[35] Daniel A. Steck. "Rubidium 85 D Line Data". In: (2008).

[36] Rudolf Grimm, Matthias Weidemüller, and Yurii B. Ovchinnikov. "Optical dipole traps for neutral atoms". In: *Advances in atomic, molecular, and optical physics* 42 (2000), pp. 95–170.

[37] D. Frese et al. "Single atoms in an optical dipole trap: Towards a deterministic source of cold atoms". In: *Physical review letters* 85.18 (2000), p. 3777.

[38] J. P. Gordon and A. Ashkin. "Motion of atoms in a radiation trap". In: *Physical Review A* 21.5 (1980), p. 1606.

[39] Wolfgang Alt et al. "Single atoms in a standing-wave dipole trap". In: *Physical Review A* 67.3 (Mar. 2003). ISSN: 1050-2947, 1094-1622. DOI: 10.1103/PhysRevA.67.033403.

[40] Matthias Schulz. "Tightly confined atoms in optical dipole traps". PhD thesis. PhD thesis, University of Innsbruck, 2002.

[41] R. Mitsch et al. "Exploiting the local polarization of strongly confined light for sub-micrometer-resolution internal state preparation and manipulation of cold atoms". In: *Physical Review A* 89.6 (2014), p. 063829.

[42] R. Mitsch et al. "Directional nanophotonic atom–waveguide interface based on spin-orbit coupling of light". In: *arXiv preprint arXiv:1406.0896* (2014).

[43] E. Vetsch et al. "Nanofiber-Based Optical Trapping of Cold Neutral Atoms". In: *IEEE Journal of Selected Topics in Quantum Electronics* 18.6 (Nov. 2012), pp. 1763–1770. ISSN: 1077-260X, 1558-4542. DOI: 10.1109/JSTQE.2012.2196025.

[44] Fam Le Kien et al. "Spontaneous emission of a cesium atom near a nanofiber: Efficient coupling of light to guided modes". In: *Physical Review A* 72.3 (2005). DOI: 10.1103/PhysRevA.72.032509.

[45] H.J. Metcalf and P. van der Straten. *Laser Cooling and Trapping.* Graduate Texts in Contemporary Physics. Springer New York, 1999. ISBN: 9780387987286.

[46] Igor Dotsenko. "Raman spectroscopy of single atoms". In: *Diplom Theses, Bonn University* (2002).

[47] Philipp Schneeweiss et al. "A nanofiber-based optical conveyor belt for cold atoms". In: *Applied Physics B* 110.3 (Mar. 2013), pp. 279–283. ISSN: 0946-2171, 1432-0649. DOI: 10.1007/s00340-012-5268-2.

[48] D. Hume et al. "Accurate Atom Counting in Mesoscopic Ensembles". In: *Physical Review Letters* 111.25 (Dec. 16, 2013). ISSN: 0031-9007, 1079-7114. DOI: 10.1103/PhysRevLett.111.253001.

[49] Fam Le Kien and A. Rauschenbeutel. "Anisotropy in scattering of light from an atom into the guided modes of a nanofiber". In: *Physical Review A* 90.2 (2014). DOI: 10.1103/PhysRevA.90.023805.

[50] Udo von Toussaint. "Bayesian inference in physics". In: *Reviews of Modern Physics* 83.3 (Sept. 2011), pp. 943–999. ISSN: 0034-6861, 1539-0756. DOI: 10.1103/RevModPhys.83.943.

[51] Christine Guerlin et al. "Progressive field-state collapse and quantum non-demolition photon counting". In: *Nature* 448.7156 (Aug. 23, 2007), pp. 889–893. ISSN: 0028-0836, 1476-4687. DOI: 10.1038/nature06057.

[52] J.-B. Béguin et al. "Generation and detection of a sub-Poissonian atom number distribution in a one-dimensional optical lattice". In: *arXiv preprint arXiv:1408.1266* (2014).

Danksagung

Ich danke Professor Arno Rauschenbeutel, der es mir ermöglicht hat meine Diplomarbeit in seiner Arbeitsgruppe zu schreiben. Besonderer Dank gilt Christoph Clausen und Philipp Schneeweiß, die sich bei Problemen und Fragen immer Zeit für mich genommen haben und mich an Ihrem großen Wissen teilhaben ließen. Auch den anderen Kollegen der Arbeitsgruppe danke ich für die angenehme Atmosphäre und das gelegentliche Beachvolleyball-Match. Meinen Bürokollegen, insbesondere Michael und Bernhard, danke ich für die interessanten Gespräche und die kontinuierliche Versorgung mit Manner-Schnitten. Schließlich möchte ich mich besonders bei meiner Familie bedanken, ohne deren Unterstützung mir das Studium nicht möglich gewesen wäre.